Red Galaxies at High Redshift

Wuyts, S.E.R.

Chapter 6

Recovering stellar population properties and redshifts from broad-band photometry of simulated galaxies: lessons for SED modeling

Abstract. We present a detailed analysis of our ability to determine stellar masses, ages, reddening and extinction values of high-redshift galaxies by modeling broad-band SEDs with stellar population synthesis. In order to do so, we computed synthetic optical-to-NIR SEDs for model galaxies taken from hydrodynamical merger simulations placed at redshifts $1.5 \leq z \leq 2.9$. Viewed under different angles and during different evolutionary phases, the simulations represent a wide variety of galaxy types (disks, mergers, spheroids). The broad-band SEDs were then fed to a standard SED modeling procedure and resulting stellar population parameters were compared to their true values. We specifically analyze how well the SED modeling reproduces masses, ages, and extinction. Disk galaxies generally show a decent median correspondence between the true and estimated mass and age, albeit with a significant scatter ($\Delta \log M = -0.05^{+0.06}_{-0.13}$, $\Delta \log age_w = -0.04^{+0.26}_{-0.27}$). During the merger itself, we find larger offsets: $\Delta \log M = -0.11^{+0.09}_{-0.14}$ and $\Delta \log age_w = -0.11^{+0.34}_{-0.25}$. $E(B-V)$ values are generally recovered well, but the estimated total visual absorption A_V is consistently too low, increasingly so for larger optical depths ($\Delta A_V = -0.48^{+0.42}_{-0.45}$ in the merger regime). The masses, ages, $E(B-V)$, and A_V of simulated ellipticals are very well reproduced.

We discuss possible biases in SED modeling results caused by mismatch between the true and template star formation history, dust distribution, metallicity variations and AGN contribution. Mismatch between the real and template star formation history, as is the case during the merging event, drives the age, and consequently mass estimate, down with respect to the true age and mass. However, the larger optical depth toward young stars during this phase reduces the effect considerably. Finally, we tested the photometric redshift code EAZY on the simulated galaxies placed at high redshift. We find a small scatter in $\Delta z/(1+z)$ of 0.030 to 0.054, depending on the template set used.

S. Wuyts, T. J. Cox, N. M. Förster Schreiber, M. Franx,
P. F. Hopkins, L. Hernquist, B. Robertson & P. G. van Dokkum

6.1 Introduction

UNDERSTANDING the growth and aging of galaxies over cosmic time requires reliable estimates of their mass, formation epoch and star formation history. With the current generation of telescopes, stellar velocity dispersion measurements can probe the gravitational potential in which the baryonic galaxy content resides out to $z \sim 1.3$ (van Dokkum & Stanford 2003; Holden et al. 2005). Beyond this redshift, gas velocity dispersions can be measured from emission lines, but do not always trace the potential due to outflows (Franx et al. 1997; Pettini et al. 1998, 2001; Shapley et al. 2003), and would lead to biased samples missing quiescent galaxies lacking emission lines in their spectra (Kriek et al. 2006). For these reasons, most studies of high-redshift galaxies have used stellar mass estimates derived by modeling of the broad-band stellar energy distribution to characterize the mass.

Since age estimates from $H\alpha$ equivalent widths (van Dokkum et al. 2004; Erb et al. 2006c) or Balmer/4000Å break strengths (Kriek et al. 2006) are very demanding in terms of telescope time and only attainable for the brightest galaxies, stellar ages as well are commonly derived from broad-band photometry.

Over the past few years, SED modeling has been proven extremely valuable in characterizing the galaxy population in the early universe (e.g. Papovich et al. 2001; Shapley et al. 2001, 2005; Förster Schreiber et al. 2004). Nevertheless, a number of assumptions are required for the limited number of datapoints (11 passbands in our case, but often less) to lead to a single solution in terms of physical properties such as stellar mass, stellar age, dust extinction, and often redshift.

First, the star formation history (SFH) is generally modelled by a simple functional form: a single burst, constant star formation, or an exponentially declining model. In reality, high-redshift galaxies show evidence of more complex SFHs, often with brief recurrent episodes of star formation (e.g. Papovich et al. 2001; Ferguson et al. 2002; Papovich et al. 2005). Second, we use the approximation of a single foreground screen of dust in accounting for the attenuation, even though in reality the dust will be distributed in between the stars. Third, we fit solar metallicity models. Although consistent with the current metallicity estimates from near-infrared (NIR) spectroscopy of high-redshift galaxies (van Dokkum et al. 2004; Erb et al. 2006a), it must be kept in mind that these measurements are currently limited to the bright end of the galaxy population. Fourth, SED modeling generally assumes a purely stellar origin of the light, while observational evidence for a substantial fraction of low luminosity AGN at high redshift has been accumulating (van Dokkum et al. 2004; Reddy et al. 2005; Papovich et al. 2006; Kriek et al. 2006; Daddi et al. 2007). They may contribute to the optical SEDs.

Finally, one adopts a certain attenuation law, initial mass function (IMF), and stellar population synthesis code. Their appropriateness at low and high redshifts is much debated.

In this chapter, we address the impact of the first four assumptions (related to SFH, dust attenuation, metallicity, and AGN) using hydrodynamical simulations of merging galaxies (see Robertson et al. 2006; Cox et al. 2006). The SPH simulations follow the star formation on a physical basis, resulting in more complex SFHs than are allowed

in typical SED modeling. They keep track of the distribution and metallicity of gas and stellar particles, allowing a determination of the line-of-sight dependent extinction toward each stellar particle separately and a knowledge of the stellar metallicity as a function of time. Here, we apply the same SED modeling that we use for observed galaxies to broad-band photometry extracted from the simulation outputs, and study how well the mass, age, and dust content of the simulated galaxies can be recovered.

The reason we use merger simulations for this exercise is threefold. First, galaxy mergers are believed to play an important role in galaxy evolution (see, e.g., Holmberg 1941; Zwicky 1956; Toomre & Toomre 1972; Toomre 1977), increasingly so at high redshift (see, e.g., Glazebrook et al. 1995; Driver, Windhorst,& Griffiths 1995; Abraham et al. 1996). Moreover, along their evolutionary path they are visible as vastly different galaxy types, allowing to test the recovery of stellar population parameters under a wide range of conditions: gas-rich star-forming disks, dust-obscured mergers, and quiescent spheroids. Finally, in Chapter 7 we will compare predictions of the color distribution and mass density of high-redshift galaxies derived from these simulations with the observed galaxy population in deep fields. A good understanding of what it is we measure with SED modeling is crucial in order to compare identical mass-limited samples of observed and simulated galaxies.

We start with a description of the simulations in §6.2. Next, we explain the methodology of our SED modeling in §6.3. §6.4 discusses how well we can measure stellar population properties when a spectroscopic redshift is available. §6.5 repeats the analysis, now leaving the redshift as an extra free parameter (i.e., fitting for the photometric redshift). Finally, we summarize the results in §6.6.

6.2 The simulations

6.2.1 Main characteristics

The simulations on which we test our SED modeling were performed by Robertson et al. (2006). We refer the reader to that paper for a detailed description of the simulations. Briefly, the simulations were performed with the parallel TreeSPH code GADGET-2 (Springel 2005). The code uses an entropy-conserving formulation of smoothed particle hydrodynamics (Springel & Hernquist 2002), and includes gas cooling, a multiphase model for the interstellar medium (ISM) to describe star formation and supernova feedback (Springel & Hernquist 2003), and a prescription for supermassive black hole growth and feedback (Springel et al. 2005b).

At the start, each simulation consists of 120000 dark matter particles, 80000 gas particles, and 80000 stellar particles. They represent two stable, co-planar disk galaxies, each embedded in an extended dark matter halo with Hernquist (1990) profile. We have realizations where the disks start with a gas fraction of 40% and 80%. Stellar masses at the start of the simulation varied from 7.0×10^9 $M_\odot$ to 2.3×10^{11} $M_\odot$ per disk galaxy. For a given virial velocity, the halo concentration, virial mass and virial radius were scaled following Robertson et al. (2006) to approximate the structure of disk galaxies at redshift $z = 3$. In practice, this means that the mass- and redshift-

dependent halo concentration measured by Bullock et al. (2001) was adopted:

$$C_{vir}(M_{vir}, z) \approx 9 \left(\frac{M_{vir}}{M_{coll,0}} \right)^{-0.13} (1+z)^{-1}, \tag{6.1}$$

where $M_{coll,0} \sim 8 \times 10^{12}\, h^{-1}\, M_{\odot}$ is the linear collapse mass at z=0, and that the following scaling relations were used for the virial mass and virial radius of the progenitors:

$$M_{vir} = \frac{V_{vir}^3}{10GH(z)} \tag{6.2}$$

$$R_{vir} = \frac{V_{vir}}{10H(z)}, \tag{6.3}$$

where V_{vir} is the virial velocity and $H(z)$ is the Hubble parameter.

We set the ages of the stars existing at the start of the simulation such as to represent a constant star formation history prior to the start of the simulation at a star formation rate (SFR) equal to that calculated in the first phases of the simulation. The corresponding stellar metallicities were then set according to the closed box model: $Z(t) = -y \ln[f_{gas}(t)]$, where $Z(t)$ is the metallicity of a stellar particle formed at time t, the yield y=0.02 and $f_{gas}(t)$ is the gas fraction of the system at the considered time. Similarly, the gas at the start of the simulation was assigned a uniform metallicity $Z_{gas}(t_S) = -y \ln[f_{gas}(t_S)]$ where t_S represents the start of the simulation, and $f_{gas}(t_S) = 0.4$ or 0.8 respectively for our 2 gas fraction runs. The closed box model represents an upper limit on the allowed enrichment by heavy elements, which in reality may be reduced by outflows or infall of metal-poor gas (Edmunds 1990). The fact that we consider 2 gas fractions guarantees a wide range of progenitor types, with ages of a few 100 Myr and $Z_{gas} = 0.004$ for $f_{gas} = 0.8$ to typical stellar ages of a gigayear and nearly solar gas metallicity for $f_{gas} = 0.4$.

The overall timespan covered by each simulation was 2 Gyr. Figure 6.1(a) illustrates a typical star formation history of one of the merger simulations. Figure 6.1(b) illustrates the build-up of stellar mass and Figure 6.1(c) presents the accretion history onto the black hole(s). We draw the time axis relative to the actual moment of merging, defined as the timestep when the two black hole particles become one, coinciding with the peak in the accretion history. Cross symbols indicate the snapshots, separated by 70 Myr, when all physical information was stored to disk.

As time progresses, the orderly rotation and star formation in the disks is disturbed by each others gravitational pull. The star formation history shows a first, but rather shallow, bump during the first passage of the disks. Next, gravitational torques enable the gas to loose angular momentum and flow to the centers where it triggers a starburst (Larson & Tinsley 1978; Noguchi 1988; Hernquist 1989; Barnes & Hernquist 1991, 1996; Mihos & Hernquist 1994, 1996). Meanwhile, part of the inflowing gas is fed to the central supermassive black holes (SMBHs). Once the SMBHs grow massive enough, they produce a luminous quasar (Sanders et al. 1988a,b; Hernquist 1989; Sanders & Mirabel 1996; Genzel et al. 1998) whose feedback halts subsequent star formation (Di Matteo et al. 2005; Springel et al 2005a), leaving a red spheroid galaxy as remnant (Robertson et al. 2006; Cox et al. 2006).

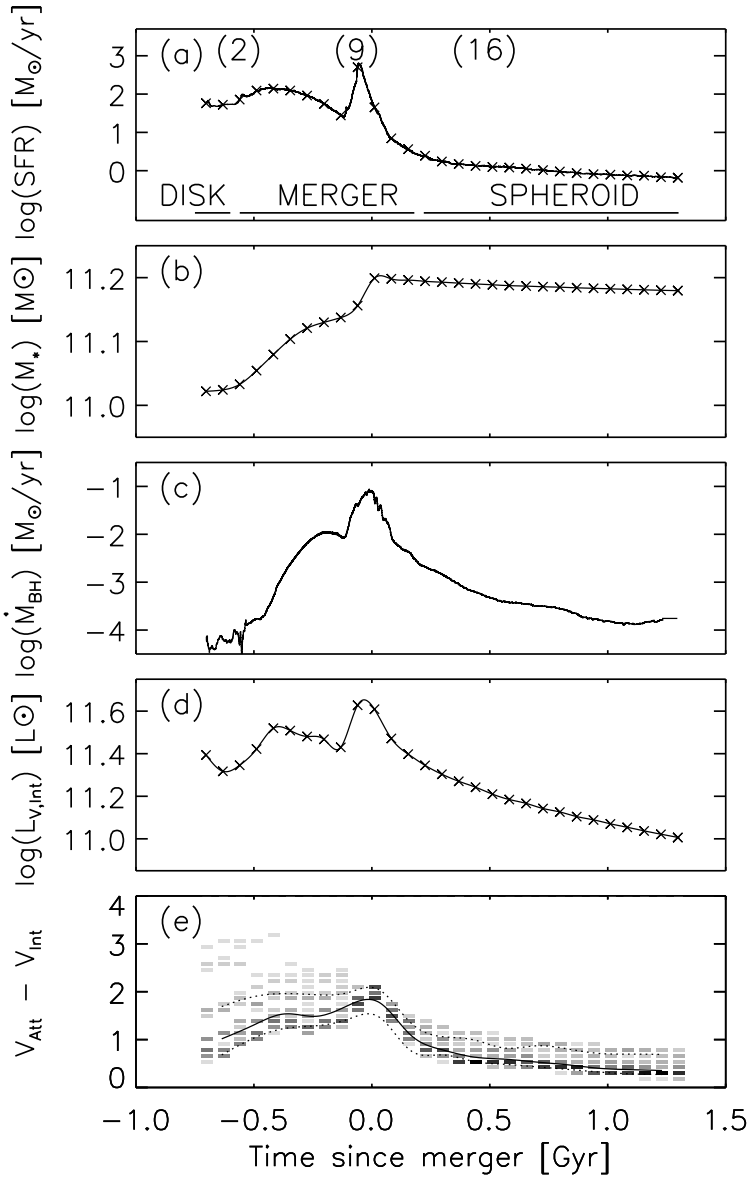

Figure 6.1 — Evolution of a typical merger simulation. (a) The star formation history, (b) the mass build-up, (c) the accretion rate history onto the black hole(s), (d) the evolution of the intrinsic (i.e., unattenuated) V-band luminosity, and (e) the binned distribution of effective visual extinctions (attenuated minus intrinsic V-band magnitude) corresponding to different viewing angles. A darker intensity indicates a larger number of viewing angles. The solid line represents the median evolution which peaks at the moment of actual merging. The dotted lines indicate the interval containing the central 68% of the viewing angles. The cross symbols in panels (a), (b) and (d) mark the sampling of snapshots when the full physical information of all SPH particles was stored to disk. After a first bump in the star formation rate during the first passage of the progenitors, a peak in star formation is reached for a brief period during which several hundreds of solar masses of gas are converted into stars. The typical extinction for a random line of sight is peaking around the same time. Shortly after, the accretion onto the supermassive black hole is maximal, coinciding with the merger between the two progenitor black holes.

6.2.2 Extracting photometry from the simulation output

The evolutionary path as outlined in §6.2.1 is followed by the GADGET-2 code at a fine time resolution ($\Delta t \sim 10^4$ yr). At sparser timesteps (70 Myr apart), the positions, masses, ages, and metallicities of all particles were stored. It is from these simulation snapshots that we derive the observed SEDs of the merger as a function of time.

The light a virtual observer would receive from the simulated merger, is composed of stellar and AGN emission, the latter only contributing significantly during a brief period of time. We ignore any contribution from emission lines produced by the gas content of the galaxies, possibly contributing on the order of 0.1 mag in the optical. Furthermore, we account for attenuation by interstellar dust and Lyman forest attenuation by the intervening medium between the redshifted galaxy and the observer following Madau (1995). The combination of these steps, described in this section, leads to observables that are similar to the real observations that we model with stellar population synthesis codes.

First, we focus on the computation of intrinsic (i.e., unattenuated) magnitudes from the stellar component. Each of the stellar particles is treated as a single stellar population characterized by its mass, age, and metallicity. We choose to use the Salpeter (1955) IMF, as was done in previous observational work (e.g. Förster Schreiber et al. 2004; Wuyts et al. 2007). We then interpolate the corresponding luminosity for each stellar particle from a grid of SSP templates with different ages and metallicities from the stellar population synthesis code by Bruzual & Charlot (2003, hereafter BC03). Figure 6.1(d) illustrates the evolution of the intrinsic rest-frame V-band luminosity for one of the simulations.

For the AGN emission, we scale a template SED by the bolometric black hole luminosity given by the simulation. The template SED was derived from the optically blue (i.e., unreddened) quasar sample by Richards et al. (2006) with locally attenuated light being reprocessed as an IR bump longward of $\lambda > 1$ μm. A full discussion of the AGN template is presented by Hopkins, Richards,& Hernquist (2007). In most of our analysis, we will consider the stellar light only. §6.4.4 addresses the impact AGN can have on the outcome of SED modeling during the brief period when its contribution to the total light is significant.

Galaxies, certainly in their actively star-forming phases, are not devoid of gas and dust. It is therefore crucial to account for the obscuring and reddening effect dust has on the stellar and AGN emission. We compute the optical depth along the line of sight toward each stellar particle. To do so, we compute the local gas density on a fine grid derived from the SPH formalism and the particle distribution (Hopkins et al. 2005a) and integrate out from each particle along the line of sight to large distance. The simulations are based on the GADGET multi-phase ISM model developed by Springel & Hernquist (2003). This model calculates the local mass fraction in the hot ($T = 10^5 - 10^7$ K, diffuse, partially ionized) and cold ($T = 10^3$ K, molecular and HI cloud core) phases of dense gas, assuming pressure equilibrium between the two phases. Following Hopkins et al. (2005b), the attenuation along the line of sight is then derived from the density of the hot-phase component only. The assumption that most of the lines of sight only pass through the hot-phase component provides effec-

tively a lower limit on the optical depths. We use a gas-to-dust ratio equal to that of the Milky Way, $(A_B/N_{HI})_{MW} = 8.47 \times 10^{-22}$ cm^2, with a linear scaling factor accounting for gas metallicities deviating from solar: $A_B/N_{HI} = (Z/0.02)(A_B/N_{HI})_{MW}$. As default, we adopt the Calzetti et al. (2000) attenuation law for the wavelength dependence of the optical depth. Changes in the synthetic photometry when adopting a SMC-like or Milky Way-like attenuation law from Pei (1992) will be discussed in due time. The computation of optical depths was repeated for 30 viewing angles, uniformly spaced in solid angle $d\cos\theta d\phi$. Figure 6.1(e) presents the distribution of effective visual extinction values (attenuated minus intrinsic V-band magnitude) as a function of time since the merger. The extinction varies in the following way. In the early stages typical extinction values are modest, with the exception for a few lines of sights were the disks are seen edge-on. The overall extinction along all lines of sight reaches a peak during the merger-triggered starburst and drops to very low values after star formation has ceased.

Finally, in computing the observer-frame apparent magnitudes, we redshift the attenuated SED and convolve it with the same set of filter curves that we have observations for in the Chandra Deep Field South (CDFS; Chapter 3). Here, we apply the depression factors $D_A(z)$ and $D_B(z)$ given by Madau (1995) for the Lyman forest attenuation of the continuum between Lyα and Lyβ and between Lyβ and the Lyman limit respectively. The flux blueward of the Lyman limit ($\lambda_L = 912$Å) was set to 0, as is done by the HYPERZ code (v1.1, Bolzonella et al. 2000) that we use for SED modeling.

In practice, it is computationally more convenient to interpolate the apparent magnitudes in a given passband for all stellar particles on a precompiled grid of BC03 apparent magnitudes at the redshift of interest. The internal dust attenuation is then applied using the value of the Calzetti et al. (2000) attenuation law at the effective wavelength for that passband. We tested that this method, as opposed to attenuating the full resolution BC03 spectrum and then convolving with the filter curve, leads to photometric differences of at most a few percent.

We note that we never attempt to separate the light into the contribution from the two progenitors. Instead, we always study the total photometry, as if the merging system were unresolved.

6.2.3 The colors and SEDs of simulated and observed galaxies

Prior to analyzing the performance of our SED modeling procedure, it is important to confirm that the simulated galaxies have spectral shapes resembling those of real high-redshift galaxies in observed deep fields, thus validating their role as test objects. To this end, we indicate the binned color distribution of simulated galaxies, viewed from different angles and during different phases of their evolution, in a rest-frame $U-V$ versus $V-J$ color-color diagram. Labbé et al. (2005) first introduced the observed-frame equivalent of this diagram to illustrate the wide range of galaxy types at high redshift ranging from blue, relatively unobscured star-forming systems to dusty starbursts to quiescent red galaxies. Plus symbols show the location of observed galaxies in the HDFS (Labbé et al. 2003), MS 1054–03 (Förster Schreiber et al. 2006), and the CDFS (Chapter 3) selected by their photometric redshift (or spectroscopic when available) to lie in the same redshift range ($1.5 < z < 3.0$). We also applied a stellar mass

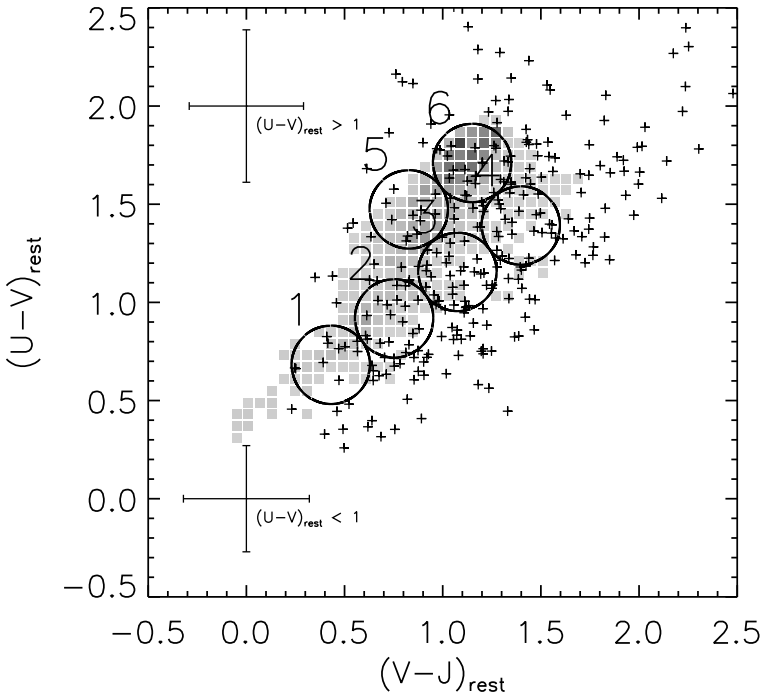

Figure 6.2 — Rest-frame $U-V$ versus $V-J$ color-color diagram showing the binned color distribution of the simulations seen under different viewing angles and at different epochs. Overplotted (*plus symbols*) are the rest-frame colors of observed galaxies with $M_* > 1.4 \times 10^{10}\ M_\odot$ at $1.5 < z < 3$ in the HDFS, MS 1054–03, and the CDFS. Observed galaxies with matching colors are found for all simulated galaxies. The reddest observed sources in $U-V$ and $V-J$ are not reproduced by the considered set of simulations. Rest-frame SEDs for sources in regions 1-6 are displayed in Figure 6.3.

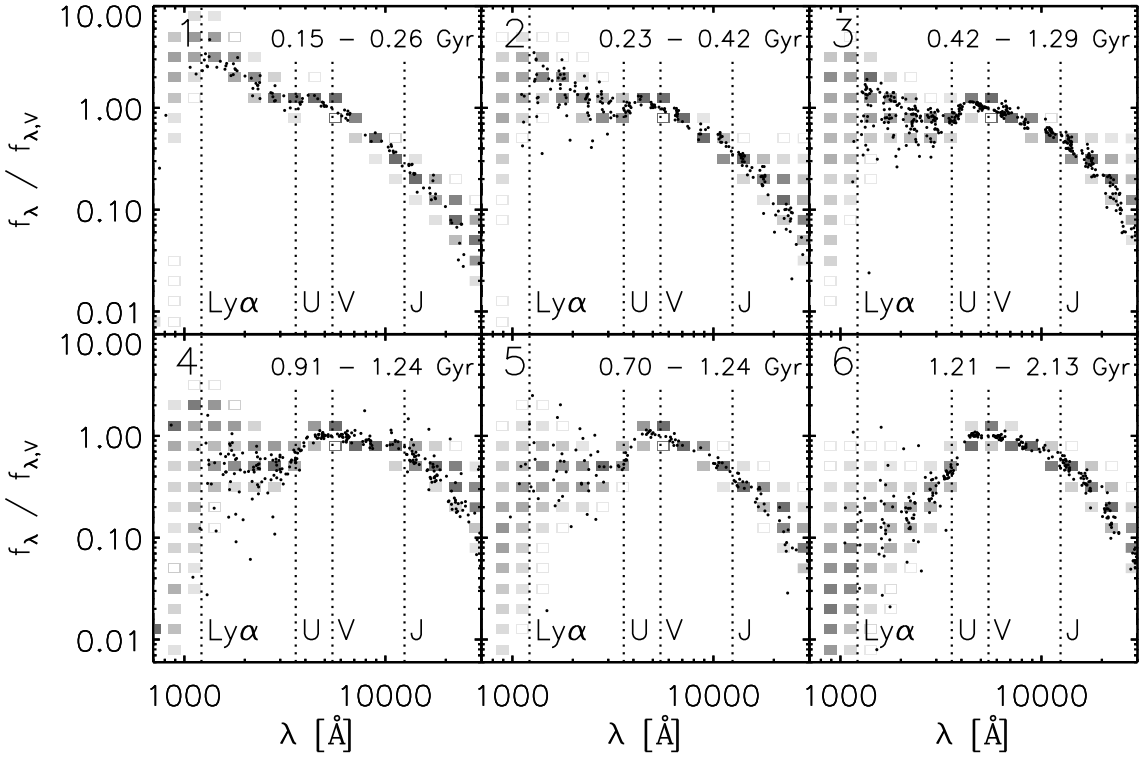

Figure 6.3 — Rest-frame SEDs of simulated galaxies in regions 1-6 of Figure 6.2. A darker intensity of the binned representation indicates a larger density of simulated galaxies with that flux level. In each panel, the central 68% interval of the age distribution of simulated galaxies in the respective region is given. Overplotted (*black dots*) are the rest-frame broad-band SEDs of observed $1.5 < z < 3$ galaxies with $M_* > 1.4 \times 10^{10}\ M_\odot$ in the HDFS, MS 1054–03, and the CDFS. A general agreement between observed and simulated spectral shapes is observed, also outside the U-to-J range where the correspondence was not imposed by selection.

cut at $M_* > 1.4 \times 10^{10}\ M_\odot$ for the observed sample; the lowest initial stellar mass for the considered set of simulations. Here, we do not attempt to statistically compare the two samples. The abundances of different types of galaxies as predicted from the simulations will be addressed in Chapter 7. For our current purpose of analyzing the effects from star formation history, dust, metallicity and AGN on SED modeling, it is sufficient to note that there is a large overlap between the color-color space spanned by the simulated and observed galaxies. However, the observed distribution extends to redder colors by a few 0.1 mag, both in $U-V$ and in $V-J$. Given the one-sided nature of the different color spread, it is unlikely that this can be attributed to photometric uncertainties alone. Therefore, we caution that our results may not necessarily be extrapolated to the reddest galaxies present in observed samples.

To ascertain that observed and simulated galaxies with similar $U-V$ and $V-J$ colors have similar SEDs over the whole spectral range, Figure 6.3 presents the rest-frame SEDs of objects in region 1-6 of Figure 6.2. Again, the binned distribution represents the simulations, with the greyscale indicating a larger number of objects. Overplotted with black dots is the broad-band photometry of our observed sample within the same region of color-color space, placed at the respective rest-frame wavelength. The SEDs are normalized to the rest-frame V-band. By selection, the observed and simulated photometry matches well at rest-frame U and J. In between the UVJ filters, and outside the U-to-J range, no correspondence was imposed. The fact that the UV spectral shape and the NIR tail of the observed and simulated SEDs show a general agreement, is encouraging. We conclude that the simulated photometry can be adopted as a realistic input to our SED modeling procedure. The results of our analysis will be applicable to observed galaxies with similar colors.

6.3 SED modeling: methodology

We characterize physical parameters such as stellar mass, stellar age, and dust attenuation by matching the observed-frame broad-band photometry to synthetic templates from the stellar population synthesis code by BC03. We use the HYPERZ stellar population fitting code, version 1.1 (Bolzonella et al. 2000) and fit the SED twice: first fixing the redshift to the true value (for which we computed the simulated photometry), next adopting a photometric redshift estimate obtained from the EAZY version 0.5 photometric redshift code (Brammer et al. in preparation). In each case, the full B-to-8 μm SED, sampled with identical passbands as available for the GOODS-CDFS (B_{435}, V_{606}, i_{775}, z_{850}, J, H, K_s, [3.6 μm], [4.5 μm], [5.8 μm], [8.0 μm]), was fed to HYPERZ. Random photometric uncertainties were assigned as to mimic real observations in the CDFS, and fluxes in each band were perturbed accordingly. Precisely, for each of the 5400 SEDs corresponding to a simulated galaxy observed during a certain phase of its evolution, placed at a certain redshift, and observed along a certain line-of-sight, we compute 5 realizations of the SED by introducing a gaussian perturbation in all bands with the amplitude derived from the depth of GOODS-CDFS observations in the respective bands. A minimum error of 0.08 mag was adopted for all bands, preventing small errors from dominating the fit.

As in Wuyts et al. (2007), we selected the least χ^2 solution out of three possible

star formation histories: a single stellar population (SSP) without dust, a constant star formation (CSF) history with dust (A_V varying from 0 to 4 in steps of 0.2), and an exponentially declining star formation history with an *e*-folding timescale of 300 Myr (τ_{300}) and identical range of A_V values. Ages were constrained to be larger than 50 Myr, to prevent improbably young ages, and smaller than the age of the universe at the observed redshift. We used a Calzetti et al. (2000) attenuation law, and assumed solar metallicity and a Salpeter (1955) IMF with lower and upper mass cut-offs $0.1M_{\odot}$ and $100M_{\odot}$.

When referring to the age derived from SED modeling, we mean the age obtained by integrating over the different ages of SSPs that build up the best-fit SFH, weighted with their mass fraction. This measure aims to quantify the age of the bulk of the stars. For an SSP, it equals the time passed since the single burst. For a CSF history, it is essentially half the time passed since the onset of star formation. The τ_{300} SFH represents an intermediate case.

6.4 Results from SED modeling at fixed redshift

In order to isolate effects from star formation history (§6.4.1), dust attenuation (§6.4.2), metallicity variations (§6.4.3), and AGN contribution (§6.4.4), we computed the photometry for each snapshot with and without attenuation, with and without AGN contribution, and using solar metallicity, or the metallicity as computed by the simulation for each stellar particle. To each of these sets of SEDs, we applied the modeling described in §6.3. In §6.4.1 - §6.4.4, we build up the analysis step by step adding one aspect at a time. The overall performance of the standard SED modeling applied to the 'full' photometry, taking into account the effects of both attenuation, metallicity, and AGN contribution as realistically as possible, is discussed in §6.4.5.

6.4.1 Impact of mismatch between true and template SFH

The contribution of massive O and B stars makes young stellar populations brighter than older stellar populations, giving them more weight in the integrated SED. Consequently, the light-weighted stellar age will be younger than the mass-weighted stellar age. This is always the case, but provided we have a template representing the correct SFH, it is possible to account for this effect and still find the correct age of the bulk of the stars. Our three allowed SFHs are an SSP, where all stars formed in a single burst, a model with $SFR \propto e^{-t/\tau}$ with τ = 300 Myr, and a constant star formation history. These are standard choices in analyses of distant galaxies. However, they do not encompass a star formation history where the rate of star formation was lower in the past than it is now, as is the case during first passage and during the actual merger-triggered starburst (see Figure 6.1). In general, fitting a template SFH that has $\left[\frac{dSFR}{dt}\right]_{template} < \left[\frac{dSFR}{dt}\right]_{true}$, the older population will be lost to some degree under the glare of newly formed stars, leading to an underestimate of the age. Since one tends to count the young light only, mass will be underestimated as well. For the same reason, models allowing for a secondary burst of star formation on top of an older stellar population were found to reveal larger total stellar masses, in particular for blue objects (Papovich et al. 2006; Erb et al. 2006b; Wuyts et al. 2007).

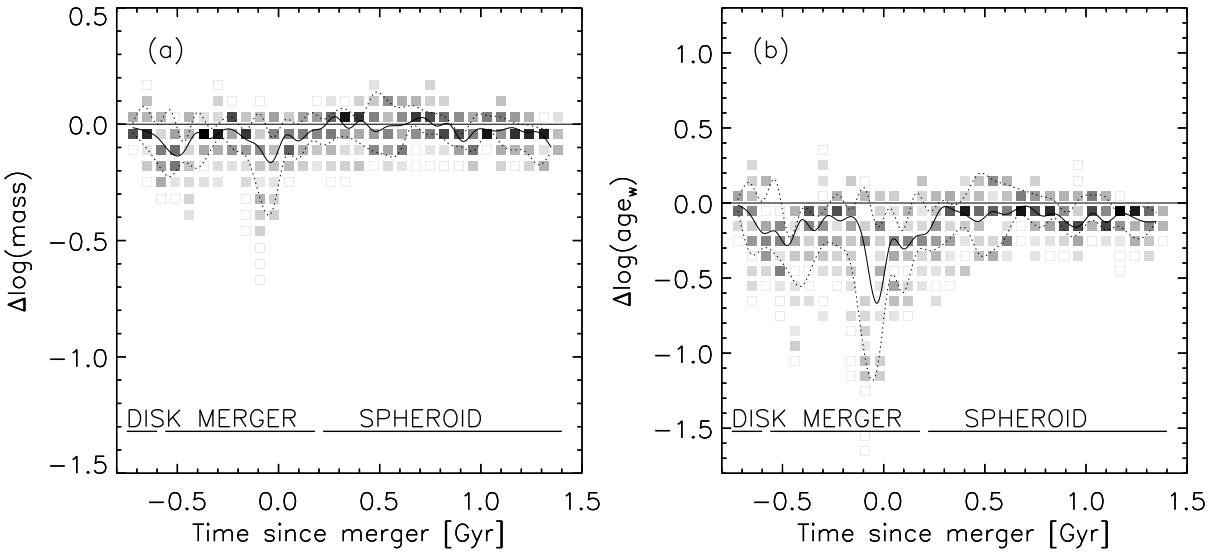

Figure 6.4 — Impact of star formation history. The difference between estimated and true (a) mass and (b) mass-weighted age as a function of time for all simulations, with the SED modeling performed on the intrinsic (i.e., unattenuated) stellar photometry with all stars set to solar metallicity. The solid line indicates the median. The dotted lines contain the central 68% of the distribution. Deviations from 0 (negative indicating an underestimate) are due to mismatch between the actual star formation history and the histories allowed in our SED modeling (SSP/CSF+dust/τ_{300}+dust). Maximum underestimates of mass and age are reached during the merger itself. A secondary minimum is reached during first passage of the progenitors, 0.3 to 0.4 Gyr before.

We demonstrate that the underestimate of mass and age takes place by considering the performance of our SED modeling procedure as applied on intrinsic stellar photometry with all stars set to solar metallicity. Here, we define $\Delta log(age_w)$ as $log(age_{w,recovered}) - log(age_{w,simulation})$. Hereafter, similar definitions will be used to quantify the offset in mass, reddening and extinction, always indicating an underestimate with a negative value of Δ. Figure 6.4 shows $\Delta log(age_w)$ as a function of time with respect to the merger between the supermassive black holes. We bin the distribution of points for different initial conditions, timesteps and lines of sight. Darker intensities represent a higher density in the bin. Open squares contain less than 1% of the total number of SEDs at that timestep. The solid line represents the median of the distribution and the dotted curves mark the central 68% interval. During the first snapshot, when the star formation history matches (by construction) our CSF template, we find no systematic offset and a low scatter, purely resulting from photometric uncertainties. Soon after, we start to underestimate the age and mass, with minima coinciding with the moment of first passage (500 Myr before the actual merger) and that of the actual merger-triggered starburst. It is precisely at these moments that the real SFH deviates most from the allowed template SFHs. During the starburst phase itself, the median offset of true mass-weighted age versus recovered age exceeds 0.5 dex, with a large scatter due to differences in the SFH for different initial conditions. For example, the ratio of SFR at first passage over SFR during the central starburst increases with gas fraction. After all activity has quieted down, the derived ages and masses lie within 0.1 dex of their true value.

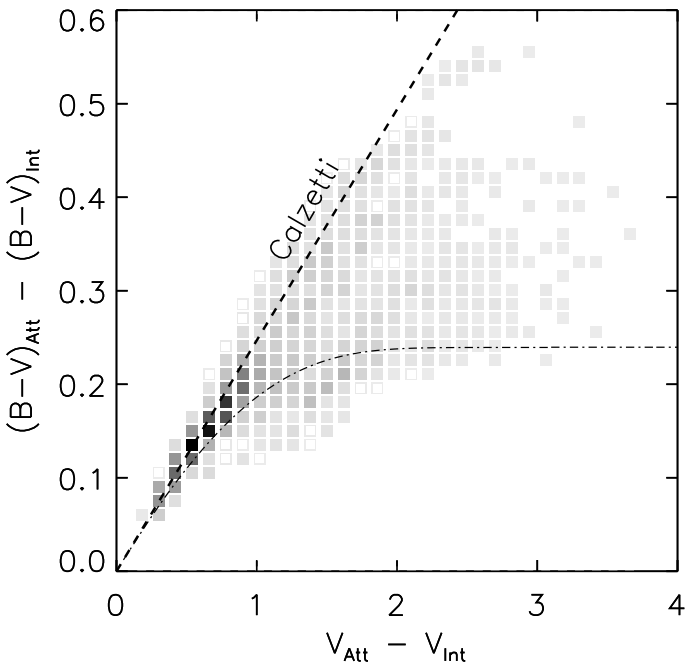

Figure 6.5 — The effective reddening (attenuated minus intrinsic $B-V$ color) versus total absorption in the V-band for all timesteps, viewing angles and initial conditions. The intensity of the binned distribution indicates the number of simulations in the respective part of the diagram. A ratio of total to selective absorption $R_V = 4.05$ as by Calzetti et al. (2000) is plotted with the thick dashed line. The dot-dashed curve indicates a toy model where the distribution of A_V values is uniform between 0 and a maximum value, and all emitting sources are identical. Stellar particles individually have $R_V = 4.05$, but in the case of a non-uniform dust distribution the sum of all stellar particles has an effective $R_V > 4.05$.

6.4.2 Impact of attenuation

As described in §6.3, we use the approach of a foreground screen to account for the attenuation by dust in our SED modeling. Figure 6.1(e), illustrating the range of effective visual extinction values (attenuated minus intrinsic V-band magnitude) for a random simulation depending on the viewing angle, proves that such a representation is not valid. Here we address the impact that a non-uniform distribution of the dust will have when modeled by a foreground screen.

First, we consider a situation where the optical depth to the stellar particles is not constant, but the variations are uncorrelated with the intrinsic properties of the stellar particles. Such a scenario is by construction the case at the start of the simulation. For each stellar particle individually the ratio of total to selective absorption,

$$R_V = \frac{A_V}{E(B-V)} = 4.05, \tag{6.4}$$

was taken from Calzetti et al. (2000). Since less extincted regions are also less reddened and have a larger weight in the integrated SED, the effective extinction $A_{V,eff} \equiv V_{Att} - V_{Int}$ and effective reddening $E(B-V)_{eff} \equiv (B-V)_{Att} - (B-V)_{Int}$ of the galaxy as a whole will not be related by the same factor 4.05 as for the individual particles. Instead, the overall reddening for a given A_V will be smaller than predicted by Calzetti (i.e., the extinction is greyer). This is illustrated in Figure 6.5 where the dashed line represents the $A_V = 4.05 \times E(B-V)$ scaling by Calzetti et al. (2000) and the dotted line represents a toy model with a uniform distribution of A_V values between 0 and A_{Vmax} to stellar particles that all emit at identical intrinsic luminosities:

$$A_{V,eff} = -2.5 \log \left[\frac{10^{-0.4 A_{Vmax}} - 1}{-0.4 A_{Vmax} ln(10)} \right] \tag{6.5}$$

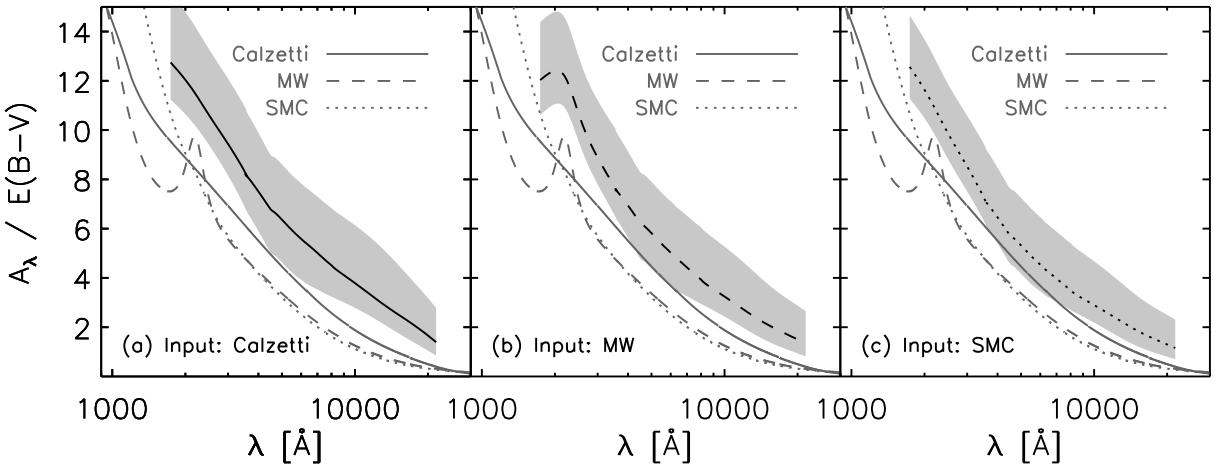

Figure 6.6 — Effective extinction curves of simulated galaxies with $A_{V,eff} > 1$ for different input attenuation laws: (a) the Calzetti et al. (2000) law, MW-like reddening from Pei (1992), and (c) SMC-like reddening from Pei (1992). The black curve indicates the median over all snapshots and viewing angles with $A_{V,eff} > 1$. The light-grey polygon indicates the central 68% interval. The Calzetti, MW, and SMC attenuation laws are plotted in grey. In all cases, the effective extinction of simulated galaxies with large $A_{V,eff}$ is greyer than the Calzetti et al. (2000) law that is used in standard SED modeling. The offset is smallest when each stellar particle is attenuated according to the SMC-like law.

$$E(B-V)_{eff} = 2.5 \log \left[\frac{\left(1 + \frac{1}{4.05}\right) \left[10^{-0.4 A_{Vmax}} - 1\right]}{10^{-0.4\left(1+\frac{1}{4.05}\right) A_{Vmax}} - 1} \right]. \tag{6.6}$$

Since the Calzetti et al. (2000) attenuation law was derived empirically for galaxies as a whole, it is arguably not the appropriate law to apply to the individual stellar particles, i.e., the smallest stellar populations that our simulation can resolve, typically $10^5 - 10^6\ M_\odot$. We investigated the changes in photometry when adopting a MW and SMC-like reddening curve by Pei (1992), which were derived in a more bottom-up fashion from the physics of interstellar dust grains. Again, we scaled the optical depth with the metallicity along the line of sight. For the SMC reddening curve, the resulting colors become redder by up to 0.05, 0.1, and 0.2 mag in rest-frame $B-V$, $U-V$, and $V-J$ respectively. The MW-like attenuation law is also less grey than Calzetti, thus producing slightly redder colors, though less so than for the SMC law. The effective extinction curve, expressed as $\frac{A_\lambda}{E(B-V)}$ as a function of wavelength, of snapshots and viewing angles with large optical depths ($A_{V,eff} > 1$) is presented for different input attenuation laws in Figure 6.6.

Not only does non-uniform extinction change the reddening ($\frac{dA_\lambda}{d\lambda}$) at a given A_V, it also affects the dependence of the reddening on wavelength ($\frac{d^2A_\lambda}{d\lambda^2}$). For extinction that is uncorrelated to the properties of the emitting sources, this gives the dust vector in the $U-V$ versus $V-J$ color-color diagram a shallower slope, i.e., for a given reddening in $V-J$, the reddening in $U-V$ is smaller than predicted by the Calzetti et al. (2000) law. The consequence of a different $\frac{d^2A_\lambda}{d\lambda^2}$ than Calzetti is clarified in Figure 6.7. The solid line represents the evolutionary track of a stellar population following a CSF history. The track starts 50 Myr after the onset of star formation and ends 2 Gyr later. Suppose different parts of a galaxy all contain a 1 Gyr old CSF population whose

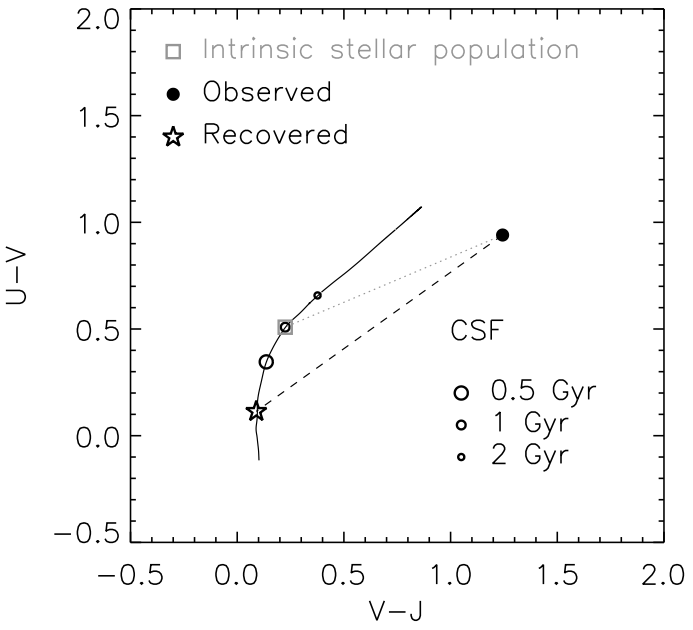

Figure 6.7 — Rest-frame $U-V$ versus $V-J$ color-color diagram illustrating the effect of a non-uniform distribution of A_V values that is uncorrelated with the intrinsic properties of the emitting sources. The black curve indicates a CSF population with age between 50 Myr and 2 Gyr. Suppose an intrinsic population (*grey square*) is reddened by such a dust distribution to the location in color-color space of the filled circle. Under the assumption of a uniform foreground screen of dust, the observed colors will then be traced back along the Calzetti et al. (2000) reddening vector (*dashed black line*), resulting in an artificially young age (*star symbol*).

intrinsic location in color-color space is marked by the grey square. A distribution of dust as described by the above mentioned toy model will redden the galaxy along the dotted line. Interpreting the observed colors (*filled circle*) as a CSF population attenuated by a foreground screen according to the Calzetti et al. (2000) law, will lead to a best-fit age (*star symbol*) that is too young and reddening that is too large.

Since in our simulations the ages of the stellar particles (that are each treated as SSPs) present at the start of the simulation were drawn randomly from a uniform distribution, the system has a CSF history in the earliest snapshots without a correlation between the optical depth and intrinsic light of the stellar particles. Therefore, it comes as no surprise that, when looking at the attenuated stellar photometry in Figure 6.8 (for now all stars still set to solar metallicity), the central 68% interval in $\Delta \log age_w$ reaches to more negative values (to -0.5 dex) during the earliest phases than was the case for the unattenuated photometry (Figure 6.4). The estimated reddening is slightly larger than the true value, but nevertheless the use of Eq. 6.4 still causes an underestimated A_V, as can be understood from Figure 6.5. The systematic underestimate in age and A_V combined cause the evaluation of the stellar mass during the first snapshots, when template mismatch due to the SFH is still negligible, to be too small by ~ 0.12 dex.

After a few 100 Myr after the beginning of the simulation however, Figure 6.8 reveals an improved recovery of the mass-weighted stellar age compared to that obtained by SED modeling of the intrinsic light (Figure 6.4). Clearly, the assumption of a non-uniform dust distribution that is uncorrelated with the intrinsic properties of the emitting sources breaks down.

Figure 6.9 demonstrates the occurence of preferential extinction toward young star forming regions in one of our simulations. The three panels indicate the binned distribution of the metallicity-scaled hydrogen column density measured along various lines of sight versus the age of the stellar particle to which the column density was computed for the 3 epochs marked in the star formation history panel of Figure 6.1.

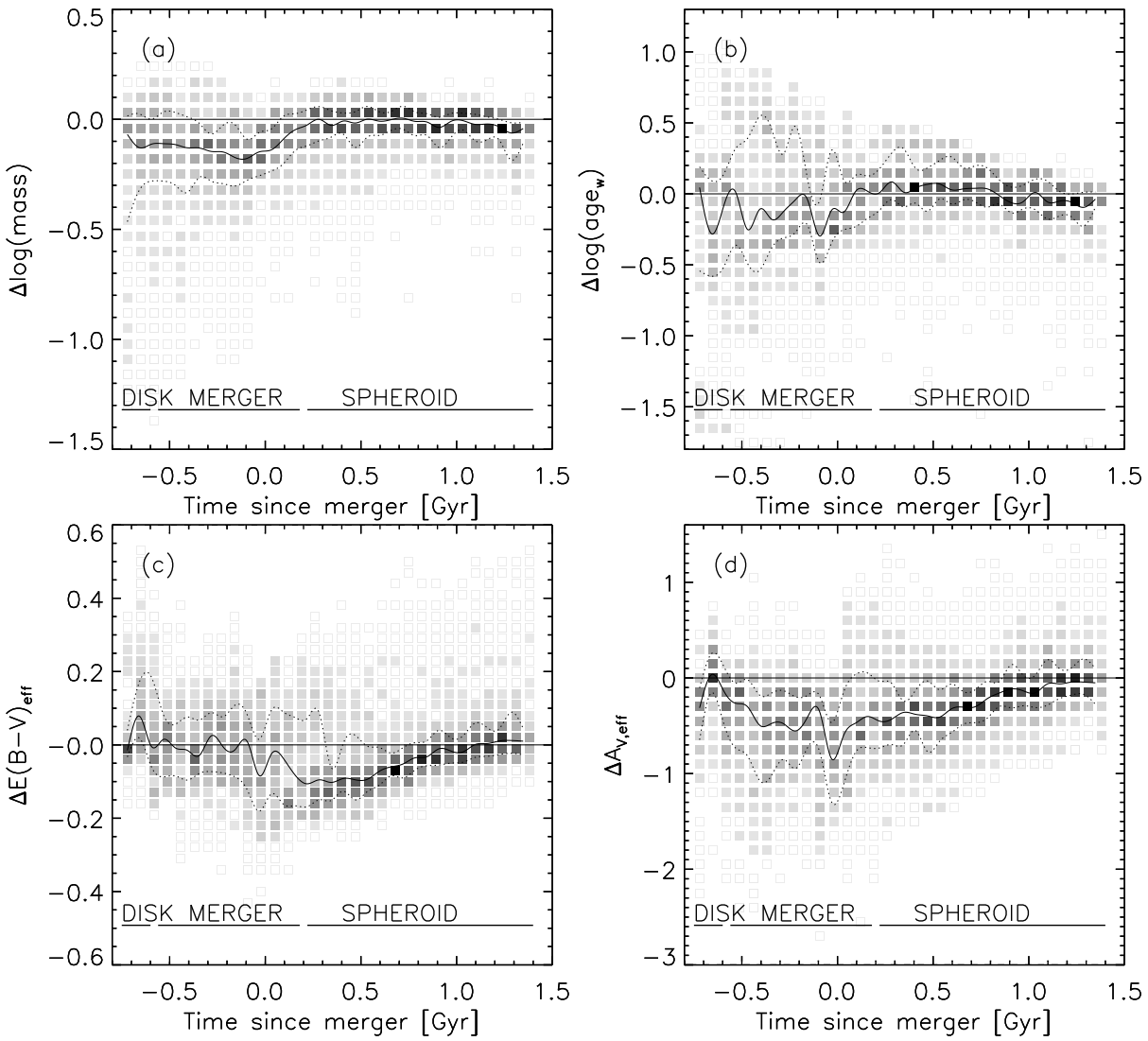

Figure 6.8 — Effect of extinction. The difference between estimated and true (a) stellar mass, (b) mass-weighted age, (c) effective reddening, and (d) effective visual extinction as a function of time since the merger. The SED modeling was performed on the attenuated stellar photometry with all stars set to solar metallicity. The solid line indicates the median and dotted lines comprise the central 68% of the distribution. Ages are still underestimated for the first 0.8 Gyr of the evolution, but to a lesser degree than estimates based on the intrinsic light. Added to the underestimated A_V, this leads to a characterization of the stellar mass that is too low by 0.1 - 0.15 dex.

The vertical arrow indicates the start of the simulation. All stellar ages older than this value (cut off for illustrational purposes) were set by hand as explained in §6.2.1. As we already pointed out in the A_V history panel of Figure 6.1, the typical column densities are higher during the merger (panel b) than before (a) or after (c). Moreover, Figure 6.9 shows that the ratio of column densities toward ongoing star formation over column densities toward older populations reaches a maximum during the merger (b). Using sticky particle simulations of dusty starburst mergers, Bekki & Shioya (2001) found a similar age-dependent extinction, confirming that this is a generic feature of merging systems and not determined by the method used to model dissipative processes.

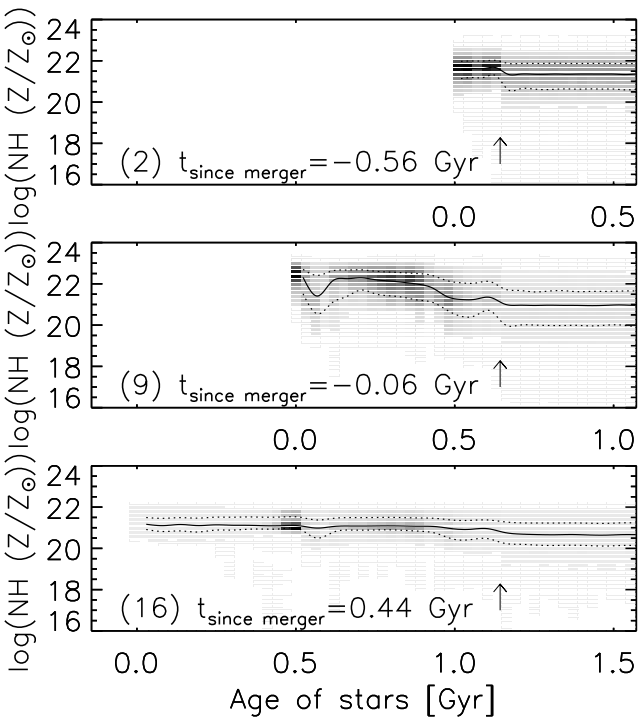

Figure 6.9 — Distribution of hydrogen column densities, linearly scaled with the metallicity of the gas along different lines of sight to the stellar particles versus the age of the respective stellar particle. The relation between column density and stellar age is plotted for 3 snapshots: before (2), during (9), and after (16) the merger (see Figure 6.1). The solid and dotted lines indicate the median and 68% interval of the distribution respectively. Darker intensity means a larger number of stars is present with that age. All stellar ages rightward of the arrow correspond to initial stars and were set by hand. The optical depth, which is proportional to the metallicity-scaled gas density, is larger toward newly formed stars during the merger-triggered starburst. The signature of this age-dependent extinction weakens during more quiescent episodes of star formation.

Poggianti & Wu (2000) inferred age-dependent extinction during a starburst to explain the nature of so-called e(a) galaxies: galaxies with [OII] in emission and strong Balmer absorption lines, frequently associated with merger morphologies.

From a physical perspective, it is expected that during the merging process hydrodynamical and gravitational forces channel gas and dust to the central regions where it triggers a starburst. Once started, supernovae going of on a few 10^7 yr timescale further increase the dust content of the regions where newly formed stars reside. The fact that the distribution of younger (and thus intrinsically bluer) stellar populations does not trace that of the older populations of stars and that it is intimately correlated with the dust distribution leads to an overestimate in age. In analogy to Figure 6.7, the effective $\frac{d^2A_\lambda}{d\lambda^2}$ is such that the galaxy is reddened along a steeper vector in the $U-V$ versus $V-J$ diagram than is the case for the Calzetti curve. Since an observer will mistakenly model the galaxy with an intrinsically redder template, the reddening by dust $E(B-V)$ will be underestimated. Although a given total absorption corresponds to a stronger reddening in the presence of age-dependent extinction compared to uncorrelated non-uniform extinction, the Calzetti et al. (2000) relation between $E(B-V)$ and A_V given by Eq. 6.4 can still be considered as an upper limit. Therefore, the total absorption will be underestimated. This is illustrated in Figure 6.5 where we plot the binned distribution of true $E(B-V)$ versus true A_V for all of our simulation snapshots, viewed under a range of viewing angles. Finally, the derived stellar mass owes its more robust character to the compensating effects of systematic offsets in age and absorption.

The effect of the larger extinction toward young stars will in practice be superposed on the effect of mismatch between template and true SFH, that prevents us from fully accounting for the difference between light- and mass-weighted stellar age (see §6.4.1).

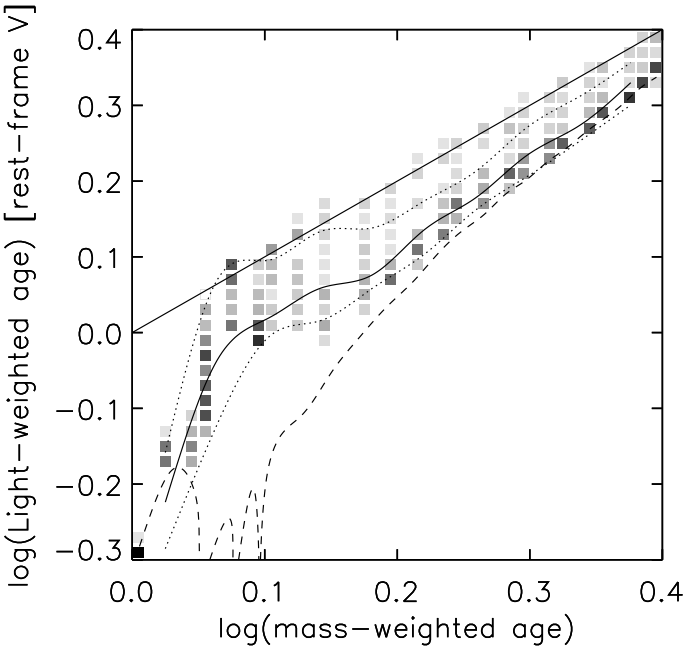

Figure 6.10 — Rest-frame V-band light-weighted age versus mass-weighted age for an initially 40% gas fraction simulation. The squares mark the mean age weighted with the attenuated V-band light. Darker intensities indicate a larger number of viewing angles. The solid and dotted curves mark the median and central 68% interval respectively. The dashed line indicates the mean age weighted with the intrinsic V-band light (no attenuation). The attenuated light-weighted age is a better approximation of the mass-weighted age than the intrinsic light-weighted age, increasingly so for younger stellar populations. Larger optical depths to young than to old stars are responsible for this effect.

Figure 6.10 illustrates how an increased extinction toward young stars reduces the difference between the light-weighted and mass-weighted measure of age. We conclude that the SED modeling on galaxies with solar metallicity stars and dust distributed in between still underestimates the age, but adding dust has improved our best guess to an overall median offset of -0.04 dex (compare Figure 6.8(b) to Figure 6.4(b)). Similar conclusions were drawn by Bell & de Jong (2001) who examine the reddening and dimming effects of dust and its impact on estimating stellar mass-to-light ratios.

6.4.3 Impact of stellar metallicity

So far, we tested our SED modeling on synthetic photometry that was computed assuming a solar metallicity for all emitting sources. In reality, stars with a range of metallicities will be present, reflecting the level of enrichment in the gas at the epoch of their formation. Before we repeat our analysis now setting the stellar metallicities to their appropriate value calculated by the GADGET-2 code, we anticipate the effect using the diagnostic $U - V$ versus $V - J$ color-color diagram in Figure 6.11.

The tracks represent exponentially declining SFHs for metallicities of Z=0.008 (*grey*) and 0.02 (solar, in *black*). Both evolutionary tracks are drawn from 50 Myr to 2 Gyr after the onset of star formation. The classic age-metallicity degeneracy states that the optical broad-band colors of a young stellar population are nearly indistinguishable from that of an older, more metal-poor population (O'Connell 1986). For the τ_{300} star formation history drawn here, this effect gets only notable at later times: 2 Gyr after the onset of star formation the sub-solar metallicity track has the same $U - V$ color as a solar metallicity population that started forming stars 1.8 Gyr ago. On the one hand, the addition of dust will complicate the age-metallicity degeneracy. On the other hand, the addition of NIR photometry helps to separate the evolutionary tracks for different metallicities. A galaxy whose attenuated light has colors marked by the filled circle may correspond with one of the intrinsic colors indicated by the grey squares depend-

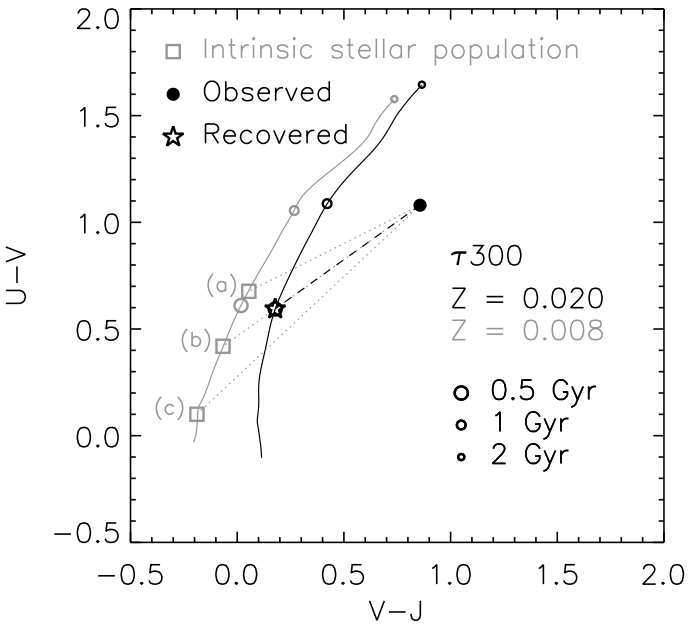

Figure 6.11 — Rest-frame $U-V$ versus $V-J$ color-color diagram illustrating the effect of fitting solar metallicity templates to stellar populations of sub-solar metallicity. The black and grey curves represent evolutionary tracks for an exponentially declining star formation history with e-folding time of 300 Myr for solar ($Z = 0.02$) and sub-solar ($Z = 0.008$) metallicity respectively, each starting at 50 Myr. Stellar populations with intrinsic colors indicated by the grey squares will be reddened to the location in color-space marked by the filled circle in the case of (a) non-uniform age-independent extinction, (b) extinction by a uniform foreground screen, and (c) age-dependent extinction. In all three cases, the assumption of solar metallicity and Calzetti attenuation will lead to the conclusion that the stellar population formed its first stars 0.5 Gyr ago. This is an underestimate (a) or overestimate (b, c) respectively. The reddening is always underestimated.

ing on the kind of extinction: (a) for non-uniform age-independent extinction, (b) for a foreground screen of dust, and (c) for age-dependent extinction. In case (a), the assumption of Calzetti attenuation and solar metallicity in our SED modeling leads to a recovered evolutionary stage that is too young, marked with the star symbol on the solar metallicity track. In case (b) and (c), the same recovered evolutionary stage is too old. In all cases, the determination of the reddening will be too low, as will consequently be the case for the A_V and the stellar mass, and increasingly so for lower metallicities. Obviously, the effects described will again be superposed on the previously discussed effects of star formation history and dust. It is also noteworthy that following the enrichment by heavy elements reduces the effect of age-dependent extinction. Young stellar populations are still intrinsically bluer than old populations, but to a lesser degree since they have formed at later times from gas that was more enriched.

In our recovery analysis of stellar population properties, we find that at metallicities of a quarter solar and below, the age is overestimated by 0 to 0.5 dex (central 68% interval of $\Delta \log age_w$). However, the underestimate in reddening and therefore extinction for these low-metallicity galaxies is such that the mass estimate (which is dependent on both age and A_V) stays within ± 0.1 dex of its true value for 68% of the cases.

6.4.4 Impact of AGN contribution

Since the merger simulations described in this chapter take into account the role of supermassive black holes on its environment (see e.g. Di Matteo et al. 2005; Springel

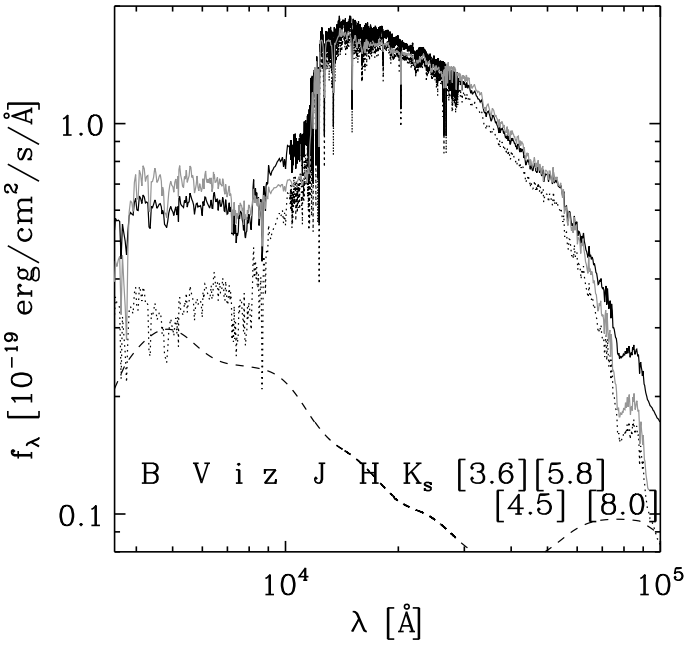

Figure 6.12 — Attenuated spectrum of a simulated merger placed at $z = 2.1$ during the peak of AGN activity. The total attenuated light (*black solid line*) is decomposed into a contribution from stars (*dotted line*) and AGN (dashed line). An observer who samples the total attenuated light with an identical set of broad-band filters as available for GOODS-CDFS and models the SED using stellar population synthesis only, will find as best-fitting model the spectrum in grey. Its age is too young by $\Delta \log age_w = -0.4$. The reddening $E(B-V)$ and absorption A_V are overestimated by 0.1 and 0.4 mag respectively. The opposite sign of offsets in age and A_V leads to a mass recovery that is only 0.05 dex below its true value.

et al. 2005b), it is straightforward to include its contribution to the integrated galaxy SED. We note that only during a timespan of the order of a Salpeter time, a few 10^7 to 10^8 year, the AGN emission amounts to a significant fraction of the stellar emission. Admittedly, the peak of AGN activity can be missed by the time sampling of our snapshots. Nevertheless, the current dataset provides a useful insight on its impact on the SED modeling.

We illustrate the typical behavior in Figure 6.12 showing the photometry computed at the time of merging when the accretion onto the supermassive black hole is maximal. Here, the solid black curve represents the light received by an observer. We break down the attenuated SED in a stellar (*dotted line*) and AGN contribution (*dashed line*). Finally, the best-fit model (in this case an exponentially declining star formation history that started 0.8 Gyr ago) is plotted in grey. Although resulting in a low $\chi^2_{reduced} \sim 1$, the SED modeling is misled by a degeneracy between the stellar+AGN light and the stellar light of a younger population obscured by large columns of dust. The addition of AGN light, when exceeding 10% of the total emission, adds another -0.1 to -0.15 dex to $\Delta \log age_w$, +0.05 to +0.1 mag to $\Delta E(B-V)$, and +0.3 to +0.5 mag to ΔA_V. These cases typically show a larger $\chi^2_{reduced}$ (70% have $\chi^2_{reduced} > 5$).

6.4.5 Overall performance

Our analysis was performed on synthetic photometry of galaxies placed at redshifts $z = 1.5$ to $z = 2.9$. The results do not show a trend with redshift. This indicates that the details of the filterset play no role. Our study only focuses on continuum shape and in the presence of spectral lines, a higher wavelength sampling in the form of spectroscopic studies will obviously provide valuable extra information. The trends described in this section are all systematic and cannot be attributed to signal-to-noise effects (e.g. more extincted galaxies at the highest redshifts being fainter and therefore less well recovered). We tested this in two ways: first by omitting the perturbation of

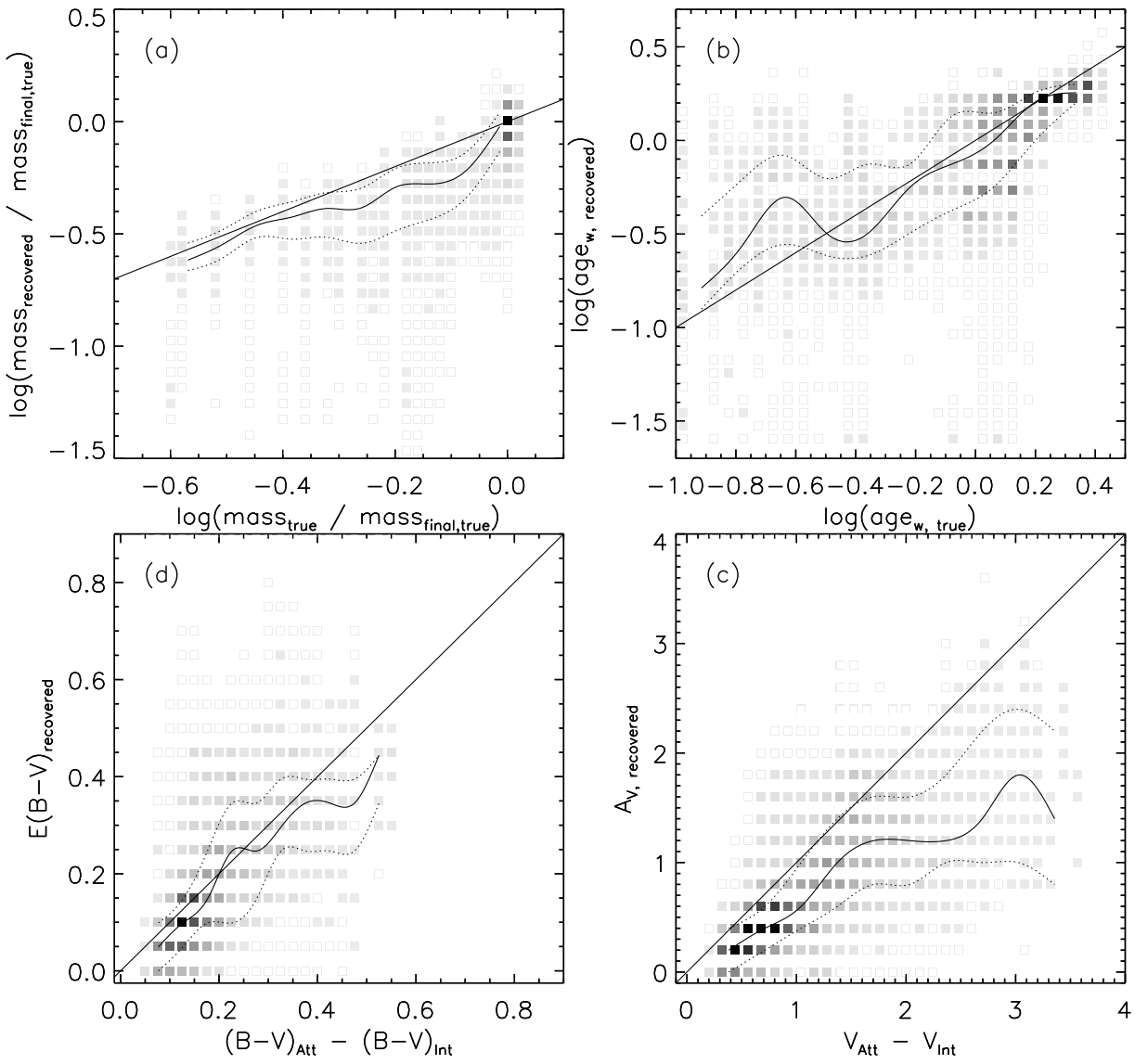

Figure 6.13 — Overall performance of the SED modeling. Recovered versus true (a) ratio of current to final stellar mass, (b) mass-weighted stellar age, (c) effective reddening (i.e., attenuated minus intrinsic $B-V$ color), and (d) effective visual extinction (i.e., attenuated minus intrinsic V-band magnitude). The SED modeling was performed on the total (stellar+AGN) attenuated photometry. The solid line indicates the median and dotted lines comprise the central 68% of the distribution. The total visual extinction A_V is the least constrained of the four studied parameters. In particular for heavily extincted galaxies the A_V is greatly underestimated.

the synthetic fluxes, second by applying a conservative cut in the observed K_s-band magnitude: $K_{s,obs} < 23.6$, corresponding to $S/N_{K_s} > 10$. In both cases, the same trends described in this section are still present.

The combined effects of mismatch in SFH, attenuation by dust, metallicity variations and AGN activity on our ability to characterize the mass, age, reddening and extinction of a galaxy is summarized in Figure 6.13. Figure 6.14 presents the performance of the SED modeling on the full photometry (including dust, metallicity variations, and

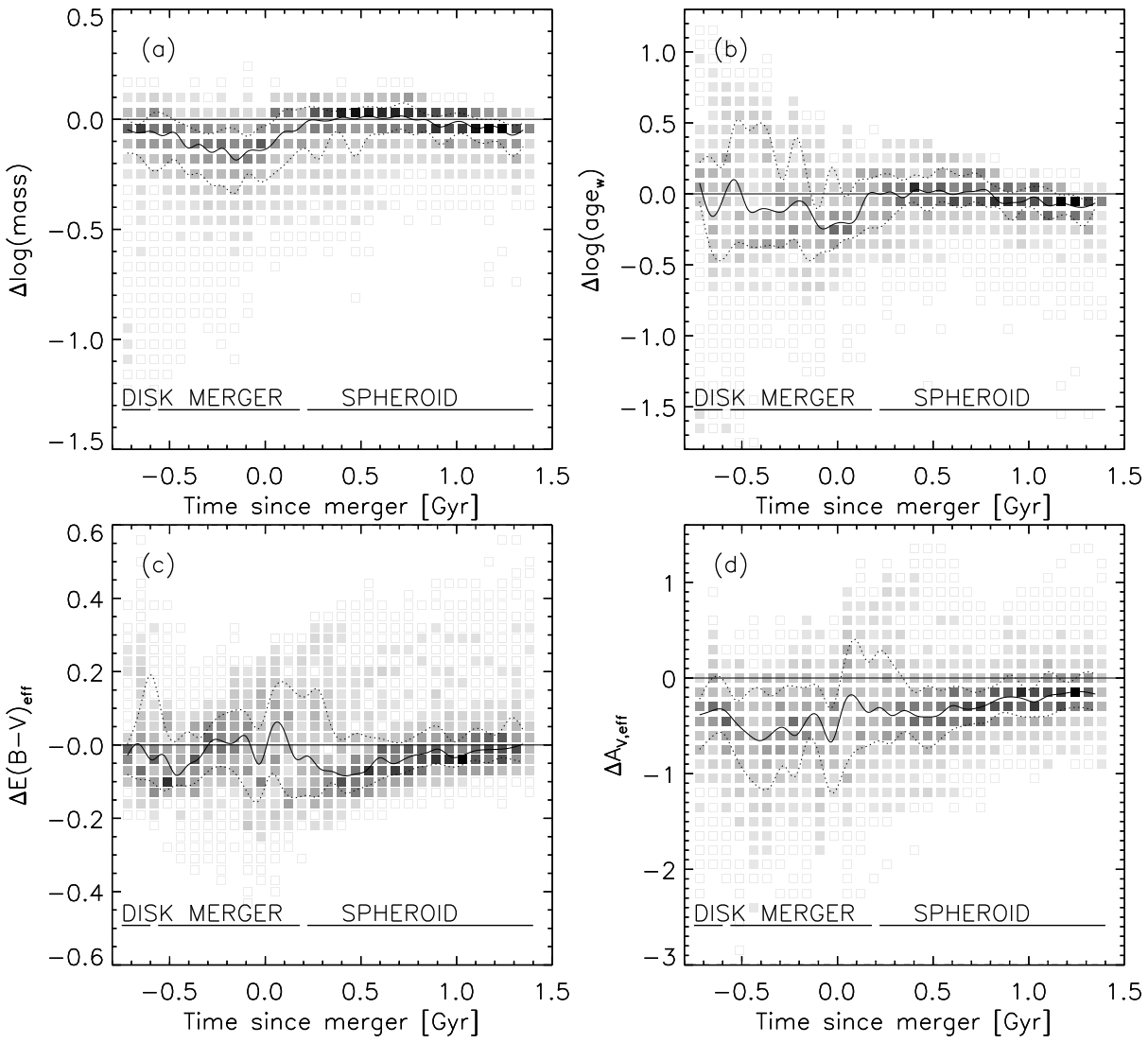

Figure 6.14 — Overall performance of the SED modeling. The difference between estimated and true (a) stellar mass, (b) mass-weighted age, (c) effective reddening, and (d) effective visual extinction as a function of time since the merger. The SED modeling was performed on the total (stellar+AGN) attenuated photometry. The solid line indicates the median and dotted lines comprise the central 68% of the distribution. The properties of merger remnants are well reproduced. The results for star-forming galaxies, especially for those in the phase of merging, show underestimates in both age, extinction, and mass.

AGN) in a different manner, as a function of time since the merger. Figure 6.13(a) compares the recovered and true stellar mass, normalized to the final stellar mass of the simulation. At low M/M_{final} ratios, i.e., at the start of the high gas fraction simulations, the mass estimates agree well with the true values. The largest systematic underestimates occur at intermediate M/M_{final}, during the merger-triggered star-forming phases of the simulation. Finally, the correspondence is best at $\log(M/M_{final}) \sim 0$, where the merger remnants reside. The same scenario is visible in Figure 6.14(a). We quantify the performance of the SED modeling separately for galaxies in the 'disk', 'merger', and 'spheroid' regime by averaging the solid (median $\Delta \log M$ as a function

of time) and dotted (central 68% interval) lines over the respective time interval indicated in Figure 6.14(a). We find $\Delta \log M_{disk} = -0.05^{+0.06}_{-0.13}$, $\Delta \log M_{merger} = -0.11^{+0.09}_{-0.14}$, and $\Delta \log M_{spheroid} = -0.01^{+0.04}_{-0.09}$. The errors indicate the range around the typical offset comprising 68% of the simulations.

Quantifying the quality of age estimates (Figure 6.13(b), Figure 6.14(b)), we find $\Delta \log age_{w,disk} = -0.04^{+0.26}_{-0.27}$, $\Delta \log age_{w,merger} = -0.11^{+0.34}_{-0.25}$, $\Delta \log age_{w,spheroid} = -0.03^{+0.10}_{-0.10}$. Again, the underestimate and scatter is largest for the phases of merger-triggered star formation. The overestimate of the youngest ages shown in Figure 6.13(b) concerns the 80% gas fraction simulations in their earliest phases, when the metallicity is low and the results from §6.4.3 apply.

The reddening (Figure 6.13(c), Figure 6.14(c)) is overall well reproduced: $\Delta E(B-V)_{disk} = -0.02^{+0.12}_{-0.07}$, $\Delta E(B-V)_{merger} = -0.01^{+0.09}_{-0.09}$, and $\Delta E(B-V)_{spheroid} = -0.04^{+0.08}_{-0.04}$. Only at the highest reddening levels, the agreement deteriorates. The latter correspond to the times when and viewing angles under which the effect of increased extinction toward young stars is maximal (see §6.4.2).

As opposed to the reddening, however, the extinction (Figure 6.13(d), Figure 6.14(d)) shows large systematic underestimates, in particular during the star-forming (disk and merger) phases. Using an R_V of 4.05 to translate the selective absorption $E(B-V)$ into a total visual absorption A_V results in an underestimate over the whole range of A_V values, particularly during the highly obscured phases. The sum of emitting sources that are each attenuated according to Calzetti et al. (2000) does not follow that same reddening law. An observer is limited by the light that he/she receives. These results are quantified as follows: $\Delta A_{V,disk} = -0.35^{+0.27}_{-0.29}$, $\Delta A_{V,merger} = -0.48^{+0.42}_{-0.45}$, and $\Delta A_{V,spheroid} = -0.27^{+0.25}_{-0.21}$.

6.4.6 Lessons for SED modeling

How can the modeling of real high-redshift galaxies benefit from our analysis of merger simulations? In order to answer this question, we need to translate the mechanisms described above in terms of the physical properties of stars and dust into their combined effect as a function of observables, such as color.

Since the results of our SED modeling showed no trend with redshift for which the synthetic photometry was computed, we can describe the quality of recovering stellar population properties in terms of rest-frame colors. Although not true observables, their computation as described by Rudnick et al. (2003) suffers from only a minor template dependence compared to parameters such as mass, age, and dust content. In Figure 6.15, we present the performance of our SED modeling as a function of location in the rest-frame $U-V$ versus $V-J$ color-color diagram. Simulations with initial gas fractions of 40% and 80% are shown separately. The SED modeling was based on the full (stellar+AGN) photometry in both cases. Downward triangles indicate a median value of $\Delta parameter$ that is negative for simulations with the respective colors. Upward triangles represent an overprediction of the true value. Lighter symbols are used for a better correspondence between the true and modeled parameter value. The different initial stellar ages and lower metallicities for $f_{gas} = 80\%$ runs explain why they extend to bluer $U-V$ colors. At blue optical colors ($U-V<1$), the attenuation is seriously underestimated. An overestimate of the age by a similar order of magnitude

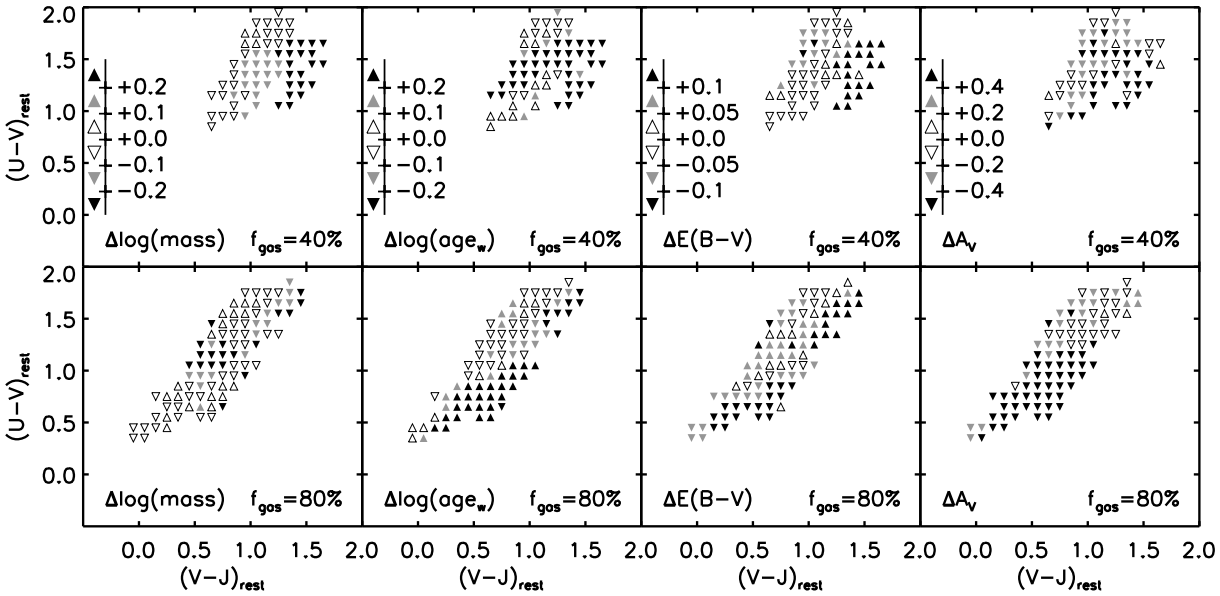

Figure 6.15 — Median quality of recovered stellar population properties for simulations with a gas fraction of 40% and 80% as a function of rest-frame optical and optical-to-NIR color. Downward triangles indicate underestimates with respect to the true value. Upward triangles mark overpredictions. Galaxies in regions with white triangles are characterized most accurately. Simulations with $f_{gas} = 80\%$ reach bluer colors in $(U-V)_{rest}$ than those with $f_{gas} = 40\%$ since their initial stars were set to younger ages (see §6.2.1). At red optical colors [$(U-V)_{rest} > 1$], galaxies with relatively blue $(V-J)_{rest}$ colors are better recovered than those at the red $(V-J)_{rest}$ end. The former are older, less obscured systems, while the latter have a young and dusty nature. At blue optical colors [$(U-V)_{rest} < 1$], large systematics in the determination of age and A_V occur. Their opposite signs cancel out in the derivation of stellar mass.

(at $U-V < 0.65$ mostly due to the lower metallicity and at $0.65 < U-V < 1$ due to age-dependent extinction) leads to a relatively robust estimate of the mass.

At red optical colors ($U-V > 1$), sources with relatively blue $V-J$ colors are generally better modeled than those with the reddest $V-J$ colors in our sample. In the $1 < U-V < 1.8$ color regime, the effects of dust attenuation play an important role. Here we find objects that are heavily extincted during the merger-triggered starburst, but also disk galaxies seen edge-on during the earliest phases of the simulation. All sources with $V-J > 1.5$ in our sample belong to the latter category. Since we did not impose an age gradient for the initial stars, the dust distribution in thoses cases is non-uniform but uncorrelated with the intrinsic color of the stellar particles. This explains why they have the strongest overestimate in $E(B-V)$. The upper part of the color-color distribution ($U-V > 1.8$) is where each galaxy ends up by aging without further inflow of gas. In such a system, the A_V values are modest to low and the lack of a template exactly matching the SFH is less problematic as the epoch of major star formation lies further back in time.

6.5 Results from SED modeling with free redshift

In practice, complete spectroscopic surveys of mass-limited samples of high-redshift galaxies are rare. Consequently, we often are not able to fix the redshift in the SED

modeling procedure to its exact true value. Over the past few years, several codes have improved on estimating the redshift based on the broad-band SED, by experimenting with different template sets and fitting algorithms. In this section, we will use the new photometric redshift code EAZY (Brammer et al. in preparation) to establish the quality of photometric redshift (z_{phot}) estimates derived from our synthetic photometry and analyze the impact of z_{phot} uncertainties on the derived stellar population properties.

6.5.1 The photometric redshift code EAZY

Here, we summarize the main characteristics of the EAZY photometric redshift code. A full description of the algorithm and template sets will be presented by Brammer et al. (in preparation). We test our ability to recover the redshifts using two template sets. The first template set is based on the same BC03 code from which the broad-band photometry of our simulations was derived (§ 6.2.2). This set consists of 10 SSP templates with a Salpeter (1955) IMF, solar metallicity, and ages logarithmically spaced between 50 Myr and 10 Gyr. Each template is allowed to have an attenuation of A_V=0.0, 0.1, 0.3, or 0.6, applied according to the Calzetti et al. (2000) law. We fit a non-negative superposition of what are effectively 40 different templates to the B-to-K_s band photometry, using a template error function that effectively downweights the rest-frame UV portion of the templates in the fit. The maximum likelihood solution is then adopted as best z_{phot} estimate.
The second setup relies on a set of hundreds of PEGASE 2.0 (Fioc & Rocca-Volmerange 1997) templates, closely matching those described by Grazian et al. (2006). The template set includes Calzetti et al. (2000) reddened CSF models to account for the presence of dusty star-forming sources. Since it is completely independent from the photometry of our simulations, it provides a check of robustness against choice of stellar population synthesis code. Given the large number of templates, we now match each template individually to the B-to-K_s band photometry, using the same template error function as for the BC03 templates.

EAZY allows for the use of a magnitude prior function, constructed from observed or simulated number counts as a function of apparent magnitude and redshift. However, since we shift each simulation over the entire redshift range $1.5 \leq z \leq 2.9$, our methodology does not allow to test this feature.

6.5.2 Recovering redshifts and stellar population properties from broad-band photometry

6.5.2.1 Recovering redshifts

In Figure 6.16, we compare the photometric redshifts obtained with EAZY+BC03 and EAZY+Pegase with the input redshifts for which the synthetic broad-band SEDs were computed. The measure commonly used to quantify the photometric redshift quality is $\Delta z/(1+z)$. Its normalized median absolute deviation is 0.030 using the BC03 template set and 0.054 using the Pegase template set. Even when using the Pegase templates, whose population synthesis is largely independent of the input photometry, the performance of EAZY is very good and competitive with that of other codes presented in

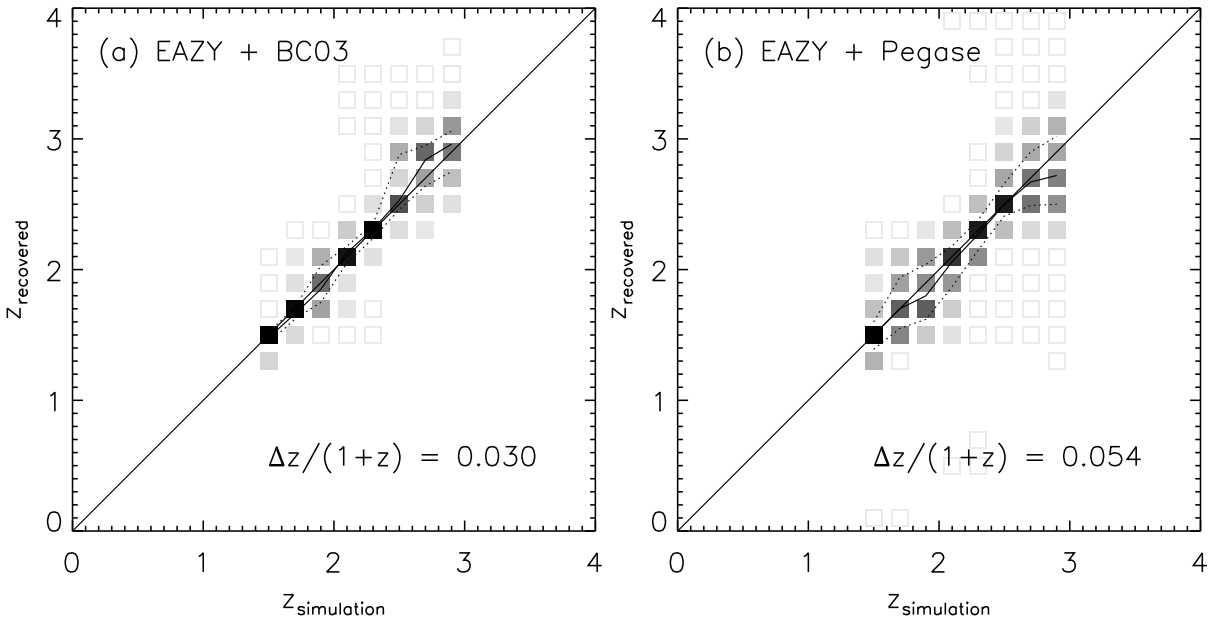

Figure 6.16 — Comparison of photometric redshift z_{phot} by EAZY versus true redshift for a template set based on (a) the BC03 and (b) the Pegase stellar population synthesis code. The correspondence is good in both cases [$\sigma_{NMAD}(\Delta z/(1+z)) < 0.06$], without significant systematic offsets. The lower scatter for EAZY+BC03 with respect to EAZY+Pegase is likely due to the fact that the input photometry is essentially a function of BC03 single stellar population templates.

the literature.

We find a correlation between $\Delta z/(1+z)$ and the time since (or before) the merger, with opposite sign for the two template sets. For EAZY+BC03, the median $\Delta z/(1+z)$ increases from -0.01 at the start of the simulation to +0.01 at the end 2 Gyr later. For EAZY+Pegase, the median $\Delta z/(1+z)$ drops from +0.02 to -0.02 over the same timespan. The correlation is with time relative to the merger (i.e., phase in star formation history) and not the stellar age. We can tell this by considering separately the 40% and 80% gas fraction simulations, which differ by their initial conditions in mass-weighted age, but show a similar dependence of the z_{phot} accuracy on time relative to the merger. No trend with A_V was found except for the reflection of the correlation with evolutionary time, i.e., the attenuation history is correlated with the star formation history (see Figure 6.1).

This exercise offers a valuable complementary test to the empirical comparison with spectroscopic samples of high-redshift galaxies. The latter are direct measurements and therefore insensitive to our knowledge of stellar tracks and population synthesis. On the other hand, spectroscopic samples of high-redshift galaxies often suffer from selection biases, especially against galaxies lacking emission lines.

6.5.2.2 Impact of z_{phot} uncertainties

Having quantified the quality of photometric redshifts, we now repeat the SED modeling fixing the redshift to its best-fit value (EAZY+BC03). The same mechanisms as discussed in §6.4 are still influencing the recovery of physical parameters. Given the par-

tially random nature of the z_{phot} uncertainties, it comes as no surprise that the central 68% interval broadens with respect to the SED modeling at fixed redshift. Averaged over time, the broadening amounts to 25%, 10%, 11%, and 15% in $\Delta \log M$, $\Delta \log age_w$, $\Delta E(B-V)_{eff}$, and $\Delta A_{V,eff}$ respectively.

The systematic part of the z_{phot} uncertainty translates into additional but small systematic offsets in the stellar population properties. Qualitatively, when a source is mistakenly placed at higher redshift, a larger mass estimate and lower dust reddening are required to match the observed SED. In numbers, the median of $\log M_{fixz} - \log M_{EAZY+BC03}$ evolves from -0.015 to +0.01 over the timespan of the simulation. $A_{V,fixz} - A_{V,EAZY+BC03}$ evolves from ~ 0 to -0.1 mag, and $E(B-V)_{fixz} - E(B-V)_{EAZY+BC03}$ from +0.01 to -0.02 mag. We find no systematic propagation of the z_{phot} uncertainty in the stellar age. Note that the impact of z_{phot} uncertainties is highly dependent on the template set used, e.g., the systematic dependence on time has the opposite sign when using Pegase templates.

6.6 Summary

We analyzed the performance of a simple SED modeling procedure applied to synthetic optical-to-NIR broad-band SEDs of merger simulations placed at redshifts z=1.5, 1.7, ..., 2.9. First, we modeled the SEDs assuming the redshift was known. The masses, ages, $E(B-V)$, and A_V of simulated ellipticals are very well reproduced, with an average value of $\Delta \log M = -0.01^{+0.04}_{-0.09}$, $\Delta \log age_w = -0.03^{+0.10}_{-0.10}$, $\Delta E(B-V) = -0.04^{+0.08}_{-0.04}$, and $\Delta A_V = -0.27^{+0.25}_{-0.21}$. Here the errors indicate the central 68% interval of the distribution of $\Delta parameter$ values of all the simulations (different masses, gas fractions, viewing angles) in the spheroid regime. In earlier, actively star-forming, phases, the scatter in recovered stellar population properties with respect to the true value increases, and larger systematic underestimates of age, mass, and extinction occur. This is particularly the case for the simulation snapshots of phases with merger-triggered star formation, where we find the following offsets and scatter (averaged over the merger regime indicated in Figure 6.1): $\Delta \log M = -0.11^{+0.09}_{-0.14}$, $\Delta \log age_w = -0.11^{+0.34}_{-0.25}$, $\Delta E(B-V) = -0.01^{+0.09}_{-0.09}$, and $\Delta A_V = -0.48^{+0.42}_{-0.45}$. The SED modeling performs better on regular star-forming disks than on galaxies during the merging event. Compared to spheroids however, the results of the SED modeling on disks show a larger scatter and larger systematic underestimates: $\Delta \log M = -0.05^{+0.06}_{-0.13}$, $\Delta \log age_w = -0.04^{+0.26}_{-0.27}$, $\Delta E(B-V) = -0.02^{+0.12}_{-0.07}$, and $\Delta A_V = -0.35^{+0.27}_{-0.29}$.

By adding the effects of dust attenuation, metallicity variations and AGN step by step to the basic intrinsic photometry, we were able to disentangle the different mechanisms at play and their impact on the estimation of the mass, age, reddening, and extinction of the galaxy. The qualitative impact on the SED modeling results by different aspects of the galaxy content is summarized in Table 6.1.

A mismatch between the real SFH and the allowed template SFHs leads to an inability to account for the difference between light-weighted and mass-weighted properties such as stellar age and mass. If the optical depth toward intrinsically bluer emitting sources is larger than to intrinsically redder stellar populations, the netto effect of the age and mass underestimate due to mismatch between true and template SFH is less

severe. We find proof of such an increased extinction toward younger stars during the merger-triggered starburst. Applying the Calzetti et al. (2000) reddening law toward each stellar particle, we find that the overall reddening for a given A_V is less than predicted by the Calzetti et al. (2000) law, particularly when the optical depth is uncorrelated with the intrinsic colors of the sources it is hiding. In the latter case, the dust vector has a shallower slope in the $U-V$ versus $V-J$ color-color diagram than the Calzetti et al. (2000) vector. In the case of larger optical depths toward young (blue) stellar populations, there is relatively more reddening in $U-V$ for a given reddening in $V-J$. Applying a MW or SMC-like attenuation law to the individual stellar particles in the simulation increases the reddening, but the effective extinction is still greyer than the Calzetti et al. (2000) law.

All other properties remaining the same, the effect of applying our SED modeling to stellar populations with sub-solar metallicities is that one would underpredict the reddening. For the young ages where such sub-solar metallicities could be expected, interpreting the light as coming from a solar-metallicity population will lead to an overestimate of the stellar age.

Finally, our SED modeling is based on purely stellar emission. During the brief period when the AGN contribution is significant, the addition of its light will make the galaxy look younger and dustier.

We next repeated our analysis adopting the best-fit photometric redshift estimate. Using the photometric redshift code EAZY (Brammer et al. in preparation) in combination with a set of BC03 templates or Pegase templates, we obtain a median normalized absolute deviation $\sigma_{NMAD}(\Delta z/(1+z)) = 0.030$ or 0.054 respectively. The random uncertainty in z_{phot} boosts the scatter in the quality measures $\Delta \log M$, $\Delta \log age_w$, $\Delta E(B-V)$, and ΔA_V, by 10-25% in the case of EAZY+BC03. A slight dependence on time with respect to the merger (opposite in sign for the two template sets) propagates into systematic differences in the estimated stellar mass, on the 6% level for EAZY+BC03 between the start and end of the simulation 2 Gyr later. Offsets in reddening and visual extinction A_V are anti-correlated with $\Delta z/(1+z)$.

Acknowledgments

We thank Eric Bell, Yuexing Li and Sukanya Chakrabarti for useful discussions in the process of writing this chapter. The hospitality of the Institute for Theory and Computation during several working visits is gratefully acknowledged. This work was supported by the Netherlands Foundation for Research (NWO), the Leids Kerkhoven-Bosscha Fonds, and the Lorentz Center.

Table 6.1. Qualitative summary of systematic trends in recovering stellar population properties.

Effect	on age	on $E(B-V)$	on A_V	on mass
SFH mismatch (higher SFR than in the past)	-	+	-	-
Non-uniform extinction (uncorrelated with intrinsic colors of emitters)	-	+	-	-
Age-dependent extinction (more extinction toward young stars)	+	-	-	-[a]
$Z < Z_\odot$	+	-	-	+[b]
AGN	-	+	+	+[c]

[a]The overestimated age and underestimated A_V compete in the determination of stellar mass. Since in practice we find this effect to be most outspoken in phases where the SFH mismatch is largest, the stellar mass will effectively be underestimated.

[b]Here too, the systematic offsets in age and A_V have an opposite sign. From comparison of mass estimates based on the full attenuated photometry and its equivalent with all stars fixed to $Z_\odot$, we find the effective $\Delta \log M$ is positive.

[c]Similar to (b), we compared the results from SED modeling with/out AGN contribution and find that in the median the addition of AGN light increases the mass estimate slightly.

References

Barnes, J. E.,& Hernquist, L. 1996, ApJ, 471, 115
Barnes, J. E.,& Hernquist, L. 1991, ApJ, 370, L65
Bell, E. F.,& de Jong, R. S. 2001, ApJ, 550, 212
Bolzonella, M., Miralles, J.-M.,& Pelló, R. 2000, A&A, 363, 476
Bruzual, G.,& Charlot, S. 2003, MNRAS, 344, 1000 (BC03)
Bullock, J. S., Kolatt, T. S., Sigad, Y., Somerville, R. S., Kravtsov, A. V., Klypin, A. A., Primack, J. R.,& Dekel, A. 2001, MNRAS, 321, 559
Calzetti, D., et al. 2000, ApJ, 533, 682
Cox, T. J., Dutta, S. N., Di Matteo, T., Hernquist, L., Hopkins, P. F., Robertson, B.,& Springel, V. 2006, ApJ, 650, 791
Daddi, E., et al. 2007, astro-ph/07052832
Di Matteo, T., Springel, V.,& Hernquist, L. 2005, Nature, 433, 604
Driver, S. P., Windhorst, R. A.,& Griffiths, R. E. 1995, ApJ, 453, 48
Edmunds, M. G. 1990, MNRAS, 246, 678
Erb, D. K., Shapley, A. E., Pettini, M., Steidel, C. C., Reddy, N. A.,& Adelberger, K. L. 2006a, ApJ, 644, 813
Erb, D. K., Steidel, C. C., Shapley, A. E., Pettini, M., Reddy, N. A.,& Adelberger, K. L. 2006b, ApJ, 646, 107
Erb, D. K., Steidel, C. C., Shapley, A. E., Pettini, M., Reddy, N. A.,& Adelberger, K. L. 2006c, ApJ, 647, 128
Ferguson, H. C., Dickinson, M., Papovich, C. 2002, ApJ, 569, 65
Fioc, M.,& Rocca-Volmerange, B. 1997, A&A, 326, 950
Förster Schreiber, N. M., et al. 2004, ApJ, 616, 40
Förster Schreiber, N. M., et al. 2006, AJ, 131, 1891
Franx, M., Illingworth, G. D., Kelson, D. D., van Dokkum, P. G.,& Tran, K. 1997, ApJ, 486, L75
Genzel, R., et al. 1998, ApJ, 498, 579
Glazebrook, K., Ellis, R. S., Santiago, B.,& Griffiths, R. 1995, MNRAS, 275, L19
Grazian, A., et al. 2006a, A&A, 449, 951
Hernquist, L. 1989, Nature, 340, 687
Holden, B. P., et al. 2005, ApJ, 620, 83
Holmberg, E. 1941, ApJ, 94, 385
Hopkins, P. F., Hernquist, L., Martini, P., Cox, T. J., Robertson, B., Di Matteo, T.,& Springel, V. 2005a, ApJ, 625, L71
Hopkins, P. F., Hernquist, L., Cox, T. J., Di Matteo, T., Martini, P., Robertson, B.,& Springel, V. 2005b, ApJ, 630, 705
Hopkins, P. F., Richards, G. T.,& Hernquist, L. 2007, ApJ, 654, 731
Kriek, M., et al. 2006, ApJ, 645, 44
Kriek, M., et al. 2006, astro-ph/0611724
Labbé, I., et al. 2003, AJ, 125, 1107
Larson, R. B.,& Tinsley, B. M. 1978, ApJ, 219, 46
Mihos, J. C.,& Hernquist, L. 1994, ApJ, 431, L9
Mihos, J. C.,& Hernquist, L. 1996, ApJ, 464, 641
Noguchi, M. 1988, A&A, 203, 259
O'Connell, R. W. 1986, in Stellar Populations, ed. C. Norman, A. Renzini,& M. Tosi (Cambridge: Cambridge Univ. Press), 213
Panuzzo, P., Granato, G. L., Buat, V., Inoue, A. K., Silva, L., Iglesias-Páramo, J.,& Bressan, A. 2007, MNRAS, 375, 640
Papovich, C., Dickinson, M., & Ferguson, H. C. 2001, ApJ, 559, 620
Papovich, C., Dickinson, M., Giavalisco, M., Conselice, C. J.,& Ferguson, H. C. 2005, ApJ, 631, 101
Papovich, C., et al. 2006, ApJ, 640, 92
Pei, Y. C. 1992, ApJ, 395, 130
Pettini, M., Kellogg, M., Steidel, C. C., Dickinson, M., Adelberger, K. L.,& Giavalisco, M. 1998, ApJ, 508, 539

Pettini, M., et al. 2001, ApJ, 554, 981
Reddy, N. A., Erb, D. K., Steidel, C. C., Shapley, A. E., Adelberger, K. L,& Pettini, M. 2005, ApJ, 633, 748
Richards, G. T., et al. 2006, ApJS, 166, 470
Robertson, B., Cox, T. J., Hernquist, L., Franx, M., Hopkins, P. F., Martini, P.,& Springel, V. 2006, ApJ, 641, 21
Sanders, D. B., Soifer, B. T., Elias, J. H., Madore, B. F., Matthews, K., Neugebauer, G.,& Scoville, N. Z. 1988a, ApJ, 325, 74
Sanders, D. B., Soifer, B. T., Elias, J. H., Neugebauer, G.,& Matthews, K. 1988b, ApJ, 328, L35
Sanders, D. B.,& Mirabel, I. F. 1996, ARA&A, 34, 749
Shapley, A. E., Steidel, C. C., Adelberger, K. L., Dickinson, M., Giavalisco, M.,& Pettini, M. 2001, ApJ, 562, 95
Shapley, A. E., Steidel, C. C., Pettini, M.,& Adelberger, K. L. 2003, ApJ, 588, 65
Shapley, A. E., Steidel, C. C., Erb, D. K., Reddy, N. A., Adelberger, K. L., Pettini, M., Barmby, P.,& Jiasheng, H. 2005, ApJ, 626, 698
Springel, V.,& Hernquist, L. 2003, MNRAS, 339, 289
Springel, V., Di Matteo, T.,& Hernquist, L. 2005a, ApJ, 620, L79
Springel, V., Di Matteo, T.,& Hernquist, L. 2005b, MNRAS, 361, 776
Toomre, A.,& Toomre, J. 1972, ApJ, 178, 623
Toomre, A. 1977, in Evolution of Galaxies and Stellar Populations, 401, Yale Univ. Obs: New Haven
van Dokkum, P. G.,& Stanford, S. A. 2003, ApJ, 585, 78
van Dokkum, P. G., et al. 2004, ApJ, 611, 703
Wuyts, S., et al. 2007, ApJ, 655, 51
Zwicky, F. 1956, Ergebnisse der Exakten Naturwissenschaften, 29, 344